

Bichromatic Tweezers for Qudit Quantum Computing in ^{87}Sr

Enrique A. Segura Carrillo  ^{1,2,*} Eric J. Meier  ² and Michael J. Martin  ^{2,3,†}

¹*JILA, National Institute of Standards and Technology and University of Colorado, Department of Physics, Boulder, Colorado 80309, USA*

²*Experimental Quantum Group, Materials Physics and Applications*

Division, Los Alamos National Laboratory, Los Alamos, New Mexico 87545

³*Center for Quantum Information and Control (CQuIC), Department of Physics and Astronomy, University of New Mexico, Albuquerque, New Mexico 87131, USA*

Neutral atoms have become a competitive platform for quantum metrology, simulation, sensing, and computing. Current magic trapping techniques are insufficient to engineer magic trapping conditions for qudits encoded in hyperfine states with $J \neq 0$, compromising qudit coherence. In this paper we propose a scheme to engineer magic trapping conditions for qudits via bichromatic tweezers. We show it is possible to suppress differential light shifts across all magnetic sublevels of the $5s5p\ ^3P_2$ state by using two carefully chosen wavelengths (with comparable tensor light shift magnitude and opposite sign) at an appropriate intensity ratio, thus suppressing light-shift induced dephasing, enabling scalar magic conditions between the ground state and $5s5p\ ^3P_2$, and tensor magic conditions for qudits encoded within it. Furthermore, this technique enables robust operation at the tensor magic angle 54.7° with linear trap polarization via reduced sensitivity to uncertainty in experimental parameters. We expect this technique to enable new loading protocols, enhance cooling efficiency, and enhance nuclear spins' coherence times, thus facilitating qudit-based quantum computing in ^{87}Sr in the $5s5p\ ^3P_2$ manifold.

I. INTRODUCTION

Neutral atoms are among the leading candidates for quantum simulation, sensing, and computing because of their long coherence times, scalability, and robustness [1, 2]. Alkaline-Earth atoms further enhance these features by introducing narrow [3, 4] and ultranarrow [5–7] lines (see Fig. 1a), which have been leveraged in narrow-line cooling schemes yielding atomic ensembles at ultracold temperatures [8–12]. Among alkaline-earth atoms, fermionic strontium, with $I = 9/2$ and dimension $d = 10$, possesses the largest nuclear spin manifold [13] (Fig. 1b). Nuclear spins in ^{87}Sr enable the development of a new qudit-based quantum computing architecture [2, 14, 15] with long coherence times [2, 16], and opportunity for error correcting protocols [17].

Optical tweezers' usefulness in assembling large atomic arrays while retaining individual atom control has made them the building blocks of neutral atom quantum computers and tweezer atomic clocks [18–23]. However, there is a trade-off: optical tweezers introduce decoherence and dephasing mechanisms [24]. Decoherence appears via Raman and Rayleigh scattering [25, 26], inducing spontaneous optical pumping, leading to leakage errors, limiting qudit coherence [17]. Dephasing emerges from nuclear-spin dependent differential light shifts, leading to gate infidelity [27].

Light shift engineering is crucial for exploiting the hyperfine degrees of freedom in the ground and excited electronic states in ^{87}Sr [14, 28]. Furthermore, it is a key component in developing information-preserving cooling

schemes [29–31], engineering new high-fidelity entangling gates [28], implementing nuclear spin state preparation, manipulation and detection protocols [32], creating novel state-selective potentials [15, 33], and assembling large, scalable, controllable, atomic arrays via optical tweezers [8, 18].

Here, we consider the possibility of using the large angular momentum $5s5p\ ^3P_2$ state for fast gate operations by leveraging its large magnetic dipole compared to $5s5p\ ^3P_0$ [14, 28]. We define our computational basis (see Fig. 1b): $5s^2\ ^1S_0(g)$ spanning nuclear spin states $|0\rangle_g = |g, m_I = -9/2\rangle, \dots, |9\rangle_g = |g, m_I = 9/2\rangle$; in $5s5p\ ^3P_2$, $F = 9/2 (e)$ the computational basis comprises hyperfine states $|0\rangle_e = |e, m_F = -9/2\rangle, \dots, |9\rangle_e = |e, m_F = 9/2\rangle$. The ratio of g -factors between these two states is $\simeq 1.1 \times 10^3$, enabling fast rf-based control of qudits stored in e . The gate speed-up in 3P_2 comes at a price: tensor light shifts in e impact coherence and limit gate times; see Fig. 2 for the tensor light shift scale induced by monochromatic light fields. Qudit-based quantum computing applications in 3P_2 require tensor light shift control to fully leverage qudits as competitive quantum computing resources.

To illustrate tweezer-induced dephasing, let us introduce the Hamiltonian defining this system as $H = H_{\text{Zeeman}} + H_{\text{LS}}$, where the Zeeman Hamiltonian is expressed as $H_{\text{Zeeman}} = g_F \mu_B \vec{B} \cdot \hat{\vec{F}}$; \vec{B} is the magnetic field vector, g_F is the Landé g -factor, μ_B is the Bohr magneton and $\hat{\vec{F}}$ is the total angular momentum operator. Next, we express the light shift Hamiltonian in its coordinate-invariant form [34] as,

* enrique.segura@colorado.edu

† mmartin@lanl.gov

$$H_{\text{LS}} = -\frac{1}{4}|E_0|^2 \left(\alpha_i^s(\omega) + \alpha_i^v(\omega) \frac{i(\epsilon \times \epsilon^*) \cdot \hat{\mathbf{F}}}{2F} + \alpha_i^t(\omega) \frac{3[(\epsilon^* \cdot \hat{\mathbf{F}})(\epsilon \cdot \hat{\mathbf{F}}) + (\epsilon \cdot \hat{\mathbf{F}})(\epsilon^* \cdot \hat{\mathbf{F}})] - 2\hat{\mathbf{F}}^2}{2F(2F-1)} \right) \quad (1)$$

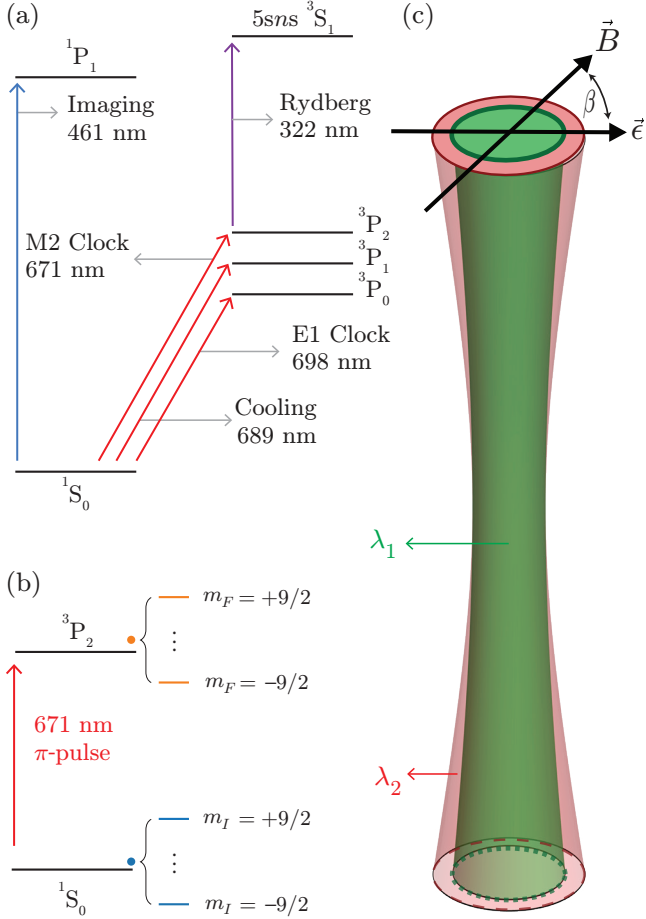


Figure 1. Light Shift Engineering in ^{87}Sr via Bichromatic Tweezer. (a) Relevant Energy Levels in ^{87}Sr for this work. (b) Representation of nuclear spins in ^{87}Sr . The nuclear spin $I = 9/2$ introduces 10 states in $^1\text{S}_0$ comprising a qudit. Through a coherent, linearly polarized, excitation at 671 nm (red line), an atom is excited to $5s5p\ ^3\text{P}_2$ for quantum operations. (c) Experimental concept of Bichromatic tweezers. By aligning the orientation of the quantization axis, defined by the magnetic field \vec{B} , relative to the polarization vector ϵ by angle β , differential light shifts between two atomic states can be manipulated.

where ω represents the angular frequency of the electric field, ϵ the polarization vector, α_i^s , α_i^v and α_i^t correspond to the bare scalar, vector, and tensor polarizabilities (see Appendix A for Eq. (A3)), E_0 the peak value of the electric field, $E_0(r=0) = \sqrt{\frac{4P}{\pi c \epsilon_0 w_0^2}}$, w_0 is the $1/e^2$ beam radius of a Gaussian beam, P is the optical power, c is the speed of light in vacuum and ϵ_0 is the vacuum permittivity.

With linearly-polarized trapping light, the α_i^t term in Eq. 1 dominates qudit dephasing, by creating unwanted

qudit operations, impacting state fidelity. Let us express the ideal polarization vector as

$$\epsilon(\beta) = [\sin \beta, 0, \cos \beta]. \quad (2)$$

In the large magnetic field limit we can neglect off-diagonal terms in this Hamiltonian of Eqn. 1, which enables magic-angle tuning, where β is set to suppress differential light shifts in a variety of settings [3, 4, 8, 35–39]. This technique enables magic trapping conditions [40, 41] in wavelengths which traditionally would not support differential light shift cancellation. For qudits, this technique provides a path for removing tensor light shifts by setting β to the tensor magic angle [42], $\beta_0 \equiv 54.7^\circ$. For quantum computing applications operating in $^3\text{P}_2$ the use of this angle for mitigating tensor light shifts requires (1) an impractical magnetic field magnitude (orders of 10^3 G) to define the quantization axis, (2) an unachievable angular precision $\delta\beta = 2 \times 10^{-5}$ radians. Furthermore, magic-angle tuning is linearly sensitive to angular fluctuations, which is compounded by the scale of light shifts present in $^3\text{P}_2$ (see Fig. 2), making operation of this technique on traditional tweezers unsuitable for qudit-based quantum computing in $^3\text{P}_2$.

In this paper we present an approach for harnessing tensor light shifts present in $^3\text{P}_2$ for engineering suitable magic trapping conditions for qudits via *bichromatic* tweezers [43–55]. We consider two bichromatic tweezer configurations: (1) a proof-of-concept configuration of two scalar magic wavelengths; (2) a combination of the $^1\text{S}_0$ – $^3\text{P}_0$ magic wavelength at 813.5 nm [56], and a complementary wavelength near 521.3 nm to yield magic trapping conditions for qudits in $^1\text{S}_0$ and $^3\text{P}_2$, a 18-state manifold. Instead of relying solely on magic-angle tuning to mitigate differential light shifts, we use two distinct colors, as depicted in Fig. 1c, at an appropriate power ratio, that together reduce total differential light shift in three ways: (1) choosing two wavelengths with opposite tensor light shift sign reduces the scale of light shifts significantly (see Fig. 2), (2) balancing intensity to eliminate the net tensor shift, and (3) finally, tuning β to β_0 with $\delta\beta = 2 \times 10^{-2}$ radians ($\delta\beta = 1^\circ$) and practical magnetic field magnitudes. Simultaneously implementing these conditions results in a highly robust tensor shift null in which off-diagonal elements of the light shift Hamiltonian are negligible, yielding an optical tweezer that is insensitive to power and angle fluctuations to second-order in these parameters.

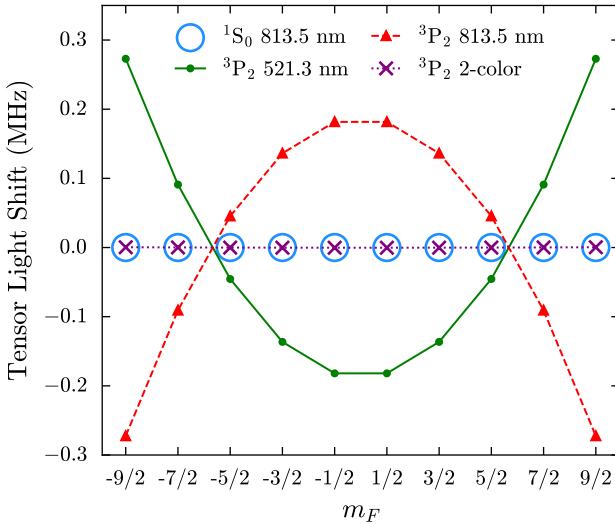


Figure 2. Flattening of the Tensor Manifold in $^3\text{P}_2$
 We illustrate the cancellation of tensor light shift induced by 813.5 nm for a laser power of 1 mW and a beam waist $w_0 = 1.0$ microns. The red dashed line with triangle markers represents the tensor light shift induced at 813.5 nm. We calculate a quadratic light shift dependency on nuclear spin m_F , which is on the scale of 0.3 MHz. The green solid line with filled circular markers represents the light shift induced in $^3\text{P}_2$ at 521 nm. The blue unfilled circles represent the light shift present in $^1\text{S}_0$ at 813 nm. The purple line with cross markers represents the resulting tensor light shift using 813 nm and 521 nm. The combined wavelengths yields a suppressed tensor light shift in $^3\text{P}_2$.

II. ENGINEERING BICHROMATIC OPTICAL TWEEZER

Our scheme tackles two challenges: (1) coherent transfer for qudits from g to e (see Fig. 1b) and (2) elimination of tweezer-induced qudit operations in e (see Fig. 2). Both concerns require light shift engineering: the former requires achieving scalar and tensor magic trapping conditions while the latter requires the elimination of tensor light shifts to preserve qudit coherence. Our technique tackles magic trapping conditions for all magnetic sublevels in e while also suppressing tensor-induced dephasing at a level of 99.9% state fidelity.

In Fig. 2 we present the incompatibility between light shifts in g , which is in the order of Hz (due to $J = 0$ suppressing tensor light shifts) and in e . This mismatch means that a qudit prepared in g and then coherently excited to e (see Fig 1b) will experience tweezer-induced dephasing from the tensor light shift. To mitigate this effect we need the following conditions: two distinct wavelengths with (1) opposite tensor polarizability sign (see Fig. A.1 in Appendix A 1), and (2) an appropriate power ratio between the two colors such that resulting differential scalar and tensor light shifts can be suppressed, yielding scalar and tensor magic trapping conditions. Realizing scalar magic trapping enables high-fidelity coherent excitation [7] to

$^3\text{P}_2$ (see Fig. 1b), while tensor magic trapping (see Fig. 2) preserves qudit coherence.

A. Effective Atomic Polarizabilities in Bichromatic Tweezers

Consider two co-propagating tweezers of two distinct wavelengths λ_1, λ_2 (see Fig. 1c) with equal beam waist w_0 , at optical powers P_1, P_2 . Furthermore, we can parametrize P_1, P_2 via an offset x between them scaled by a nominal power P [47, 57],

$$P_{1,2} = (1 \pm x)P \quad (3)$$

Let us define the scalar magic condition,

$$|\alpha_g^s(\lambda) - \alpha_e^s(\lambda)| = 0 \quad (4)$$

where $\alpha_i^s(\lambda)$ represents the bare scalar polarizability; see Eq. (A3) in Appendix A. For an electronic state i (in this context, for g, e), λ is the target wavelength that yields the minimal differential scalar polarizability. These conditions allow us to frame the search for viable parameters for the bichromatic tweezer as a light shift minimization problem. We can define the total scalar light shift in an electronic state as

$$\bar{\alpha}_i^s(\lambda_1, \lambda_2, x) = (1 + x)\alpha_i^s(\lambda_1) + (1 - x)\alpha_i^s(\lambda_2) \quad (5)$$

and total tensor shift

$$\bar{\alpha}_i^t(\lambda_1, \lambda_2, x) = (1 + x)\alpha_i^t(\lambda_1) + (1 - x)\alpha_i^t(\lambda_2), \quad (6)$$

where $\alpha_i^t(\lambda)$ represents bare tensor polarizability; see Eq. (A3) in Appendix A.

Individually these conditions provide the framework to engineer either scalar magic or tensor magic potentials. For our application, we require both scalar and tensor magic,

$$\bar{\alpha}_e^s(\lambda_1, \lambda_2, x_0) = \bar{\alpha}_g^s(\lambda_1, \lambda_2, x_0) \quad (7)$$

and

$$\bar{\alpha}_e^t(\lambda_1, \lambda_2, x_0) = \bar{\alpha}_g^t(\lambda_1, \lambda_2, x_0) \quad (8)$$

In Eq. (8) we set the total tensor shift to zero given the scale of tensor polarizability in $^1\text{S}_0$ is on the order of 10^{-5} atomic units (a.u.) [58]. The resulting configuration $\lambda_1, \lambda_2, x_0$ yields an optical potential that is scalar and tensor magic for all m_F in a hyperfine state. We define x_0 as the magic power ratio between the two wavelengths to engineer magic trapping conditions.

This framework illustrates the primary feature that a bichromatic potential provides for light shift engineering: the decoupling of the internal degrees of freedom of an atom via tuning parameters $(x, \lambda_1, \lambda_2)$. These parameters enable $\bar{\alpha}_i^t(\lambda_1, \lambda_2, x) \approx 0$ (realizing the limit where H_{Zeeman}

dominates), in the perturbative regime for a wide range of magnetic fields. Our technique's approach to realizing the perturbative regime is predicated on scaling *down* the tensor component of the light shift Hamiltonian (making it effectively zero) rather than on scaling *up* the magnetic field amplitude (necessary for magic-angle tuning).

We now consider the angle sensitivity of magic-angle tuning in the perturbative regime. Light shift suppression relying solely on β sets angle precision as the bottleneck for robust magic-angle tuning. We can describe the light shift sensitivity due to angle fluctuations,

$$\left| \frac{\partial E_{\text{LS}}}{\partial \beta} \right| \propto I_0 \sin(2\beta) \times \tilde{\alpha}_i^t \quad (9)$$

where I_0 is the total tweezer beam intensity; for a monochromatic tweezer $\tilde{\alpha}_i^t = \alpha_i^t(\lambda)$ and for a bichromatic tweezer $\tilde{\alpha}_i^t = \tilde{\alpha}_i^t(\lambda_1, \lambda_2, x)$. Using Eq. 9 we determine that light shift cancellation via bichromatic tweezers suppresses the total tensor light shift, where the overall scaling with $\tilde{\alpha}_i^t$ is apparent. Thus the bichromatic approach vastly reduces the effect of angle fluctuations and enables the operation of the tensor magic angle at practical experimental angular precision.

In the following sections of this paper we assert the following experimental conditions used for results presented in this paper: (1) beam waists are equal for both wavelengths with a beam radius of 1 micron, and (2) the time scale of 1 millisecond is used for all state fidelity calculations. Finally, we note that in this paper we calculate the magic wavelength [56] for 3P_0 to be 813.46504 nm using available reduced dipole matrix elements in the literature [5, 8, 59]. Lastly, we allow for systematic offset on wavelengths in the vicinity of 500 nm of 100 MHz.

B. Bichromatic Tweezers in 3P_2

In this section we present two configurations for engineering bichromatic tweezers in 3P_2 : 891.5 nm and 518.0 nm and 813.5 nm and 521.3 nm (the magic wavelength derived from our model) and 521.3 nm.

To illustrate the role of intensity compensation in removing tensor light shifts, we find two suitable scalar magic wavelengths (for g and e) near 891.5 nm and 518.0 nm. Choosing scalar magic wavelengths reduces the task to a tensor light shift minimization problem using Eq. (8), enabling the estimating of the appropriate power ratio to cancel out tensor light shifts. In Fig. 3a we present a bichromatic tweezer using 891.5 nm and 518.0 nm. In Table II C we present the optical powers to yield scalar and tensor magic for nuclear spins in both electronic states. We estimate a trap depth of 144 μK .

Now we turn our attention the engineering of a bichromatic tweezer in which one of its wavelengths is at 813.5 nm. Qudit readout is a crucial component in our quantum computing scheme. The 3P_0 magic wavelength at 813.5 nm [60] is a suitable wavelength for shelving atoms

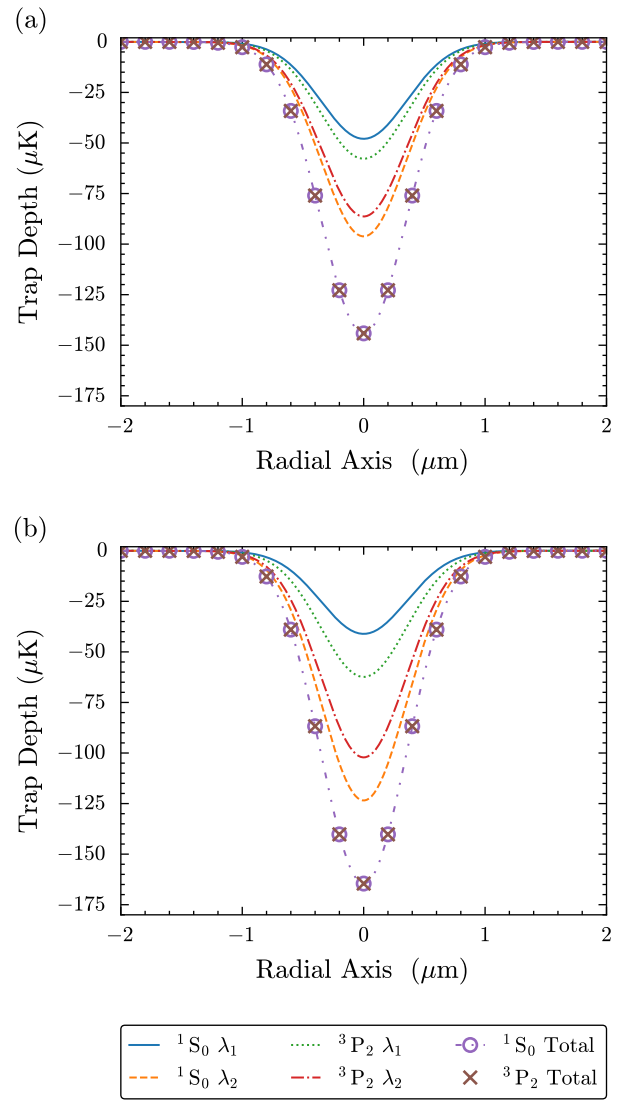


Figure 3. **Bichromatic Tweezer Configurations in ${}^{87}\text{Sr}$** ${}^3\text{P}_2$. (a) Bichromatic tweezer using 891.5 nm and 518.0 nm for ${}^1\text{S}_0 - {}^3\text{P}_2$. In this figure $\lambda_1 = 891.5$ nm and $\lambda_2 = 518.0$ nm. The solid blue and the dotted green lines represent the optical potential contributions at 891.5 nm for ${}^1\text{S}_0$ and ${}^3\text{P}_2$ respectively. The red dash-dot and the orange dashed lines represent the contributions for 518.0 nm for ${}^3\text{P}_2$ and ${}^1\text{S}_0$ respectively. The total potential for ${}^1\text{S}_0$ is presented by the purple dashed line with unfilled circles and for ${}^3\text{P}_2$ is presented by brown cross markers. (b) Bichromatic tweezer using 813.5 nm and 521.3 nm for ${}^1\text{S}_0 - {}^3\text{P}_2$. In this figure $\lambda_1 = 813.5$ nm and $\lambda_2 = 521.3$ nm. The solid blue and the dotted green lines represent the optical potential contributions at 813.5 nm for ${}^1\text{S}_0$ and ${}^3\text{P}_2$ respectively. The red dash-dot and the orange dashed lines represent the contributions for 521.3 nm for ${}^3\text{P}_2$ and ${}^1\text{S}_0$ respectively. The total potential for ${}^1\text{S}_0$ is presented by the purple line with unfilled circles and for ${}^3\text{P}_2$ is presented by brown cross markers.

in ${}^3\text{P}_0$ under magic trapping conditions, while individual atoms are probed via the broad-line transition at 461 nm.

In all cases we consider, 813.5 nm will be state readout and detection tweezer wavelength. In the 813.5 nm/521.3 nm bichromatic configuration, this readout stage is accomplished by the extinction of the 521.3 nm tweezer. In the 891.5 nm/518.0 nm configuration this is accomplished through coherent transfer to an 813.5 nm tweezer. In Table II C the optical power parameters in a bichromatic tweezer using 813.5 nm and 521.3 nm (see Fig. 3b). We calculate a trap depth of 164.56 μK and radial and axial trapping frequencies ω_r , ω_a of 53.33 kHz and 5.09 kHz respectively.

C. Experimental Tolerances Requirements for Qudit Manifold Fidelity in Bichromatic Tweezers

The challenge of using a monochromatic tweezer in $^3\text{P}_2$ lies in the scale of the tensor light shifts. Our technique enables us to leverage both the light shift cancellation achieved by using two wavelengths, which scales down the effective tensor polarizability, at a specific power ratio, which enables the operation at the tensor magic angle at practical magnetic fields. In this section we will estimate the necessary power offset tolerances to maintain a state fidelity of 0.999 at an angular precision of 1° . In what follows, we find that frequency accuracy of the tweezer beams at the level of 100 MHz does not impact yielding our target state fidelity.

We can estimate state fidelity via the Hilbert-Schmidt distance [61, 62],

$$\mathcal{F} = \frac{1}{d(d+1)} \left(|\text{Tr}\{e^{iH_{\text{Target}}t} e^{-iH_{\text{Realized}}t}\}|^2 + d \right) \quad (10)$$

where d represents dimension ($d = 10$) of the computational basis, the target Hamiltonian is defined by the Zeeman Hamiltonian, and the realized Hamiltonian is defined as $H_{\text{Realized}} = H_{\text{LS}} + H_{\text{Zeeman}}$.

x	λ	P_i	$\delta P_i/P_i$
0.2573	$\lambda_1 = 891.5 \text{ nm}$	1.257 mW	4.2×10^{-3}
	$\lambda_2 = 518.0 \text{ nm}$	0.743 mW	7.1×10^{-3}
7.467×10^{-4}	$\lambda_1 = 813.5 \text{ nm}$	1.001 mW	4.2×10^{-3}
	$\lambda_2 = 521.3 \text{ nm}$	0.999 mW	4.3×10^{-3}

Table I. Power Stability for Bichromatic Tweezers in $^1\text{S}_0 - ^3\text{P}_2$. The fractional power uncertainty for each beam is calculated by estimating the power ratio resolution δx . We define $\delta P_i/P_i = \delta x/(1 \pm x)$, where $P_i = (1 \pm x)P$ represents the optical power of each color weighted by $P = 1 \text{ mW}$. These values only assume $\delta\beta = 1^\circ$.

In Fig. 4 we present the power ratio precision needed for yielding a bichromatic tweezer using two suitable scalar magic wavelengths. This figure is obtained by tuning the power ratio uncertainty δx over a range of 5000 points

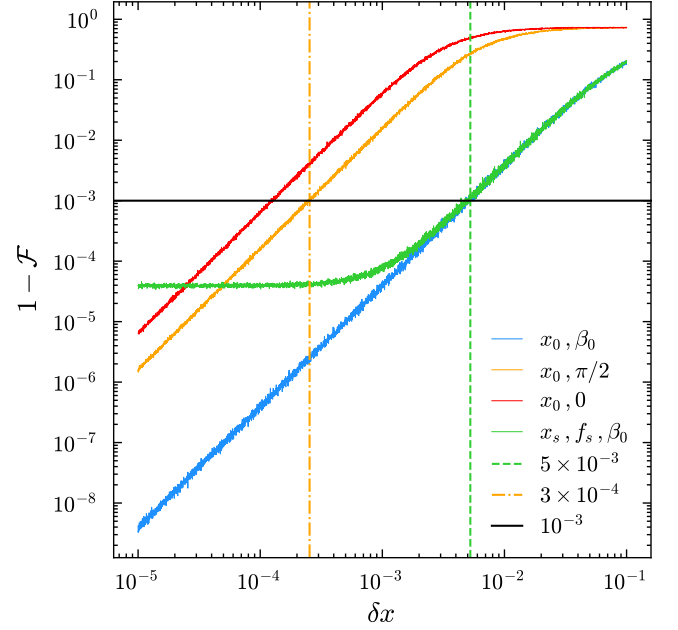


Figure 4. **State Infidelity as a Function of Power Ratio Precision for Bichromatic Tweezer using 891.5 nm and 518.0 nm.** We estimate the average state fidelity via a Monte Carlo simulation over 1000 trials per base point (5000 points spanning from $\delta x = 10^{-5}$ to 10^{-1}). The blue line represent estimated state fidelity at (x_0, β_0) . The orange line represents estimated state fidelity at $(x = x_0, \pi/2)$. The green line represents the state fidelity at $(x = x_0 + x_s, \beta_0)$. The red line represents the state fidelity at $(x = x_0, \beta_0)$. The green vertical line represents value for δx to yield $\mathcal{F} = 0.999$ for $(x = x_0 + x_s, \beta_0)$. The orange vertical dash-dotted line represents δx to yield $\mathcal{F} = 0.999$ for $(x = x_0, \pi/2)$. Finally, the black horizontal line represents target fidelity $\mathcal{F} = 0.999$.

spanning from 10^{-5} to 10^{-1} . We assume uncertainties $\delta x, \delta\beta$ to be gaussian (these values represent the standard deviation used to sample a random error around x, β) used to compute state fidelity. Furthermore we considered a systematic offset error in the power ratio $x_s = 1 \times 10^{-3}$ to estimate the impact on imperfections in relative power stabilization of the tweezer beams (such that the value used for estimating the impact of gaussian error is $x = x_0 + x_s$) as well as a systematic frequency offset $f_s = 100\text{MHz}$ for 518.0 nm to account for imperfection on laser stabilization (e.g. wavemeter calibration offsets). Moreover, we note that all configurations in the plot assume $\delta\beta = 1^\circ$. For each point δx in this range, for a fixed $\delta\beta$, we estimate fidelity out of an average of 1000 trials. For this configuration we calculate the required fractional power uncertainties (at β_0) to be 4×10^{-3} and 7×10^{-3} for 891.5 nm and 518.0 nm respectively. For the configuration using 813.5 nm and 521.3 nm we find that by operating at β_0 a state fidelity of 0.999 can be realized a fractional power uncertainty of 4×10^{-3} . We note that operating at $\beta \neq \beta_0$ (such as $\beta = \pi/2$) increases the demands in power stabilization due to the increased

loss (see vertical orange dashed line in Fig. 4) of the compounded cancellation by operating *simultaneously* at x_0, β_0 .

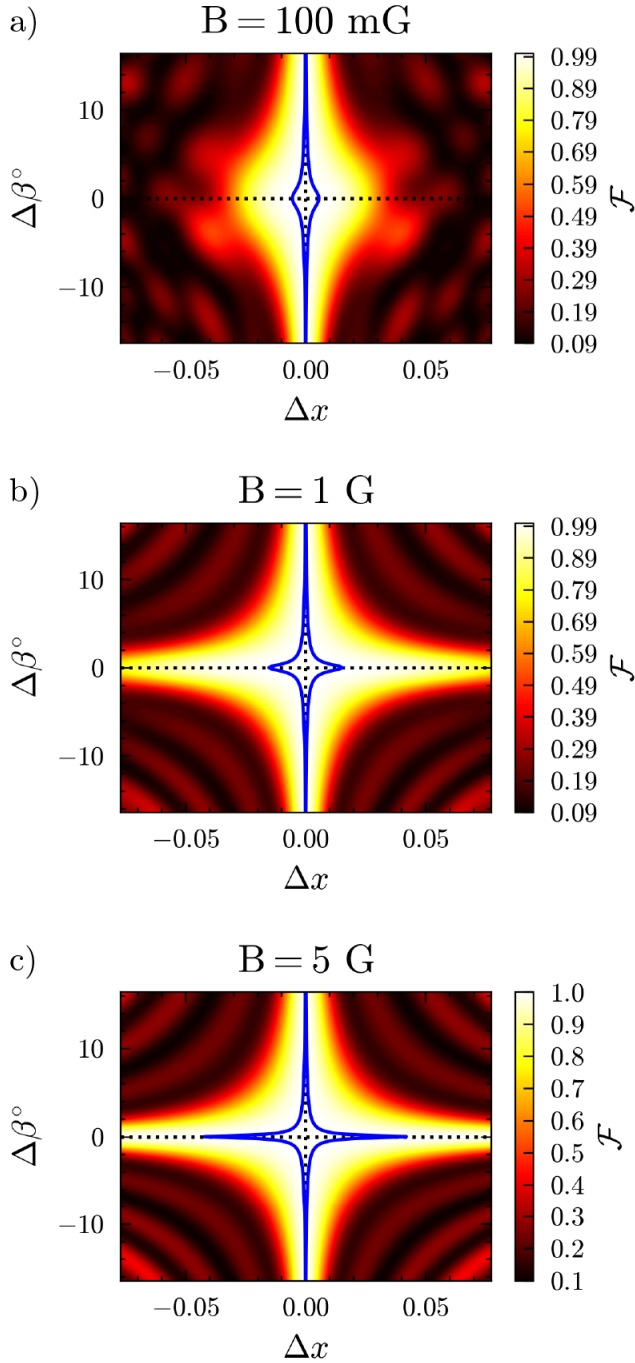


Figure 5. State Fidelity as Function of Power Ratio and Quantization Axis for 1 ms. State fidelity (a) at $B = 0.1$ G, (b) $B = 1$ G, (c) $B = 5$ G. The dashed horizontal line represents the tensor magic angle while the dotted vertical line represents the optimal power ratio. The region in the center represents the fidelity plateau. The blue contour represents the target fidelity of 0.999.

Armed with Eq. (10) we can map the parameter space to estimate the response of fidelity as a function of offset $\Delta x, \Delta \beta$ from the optimal parameters x_0, β_0 for a fixed magnetic field. In Fig. 5 we present three different magnetic fields and its impact on fidelity for the configuration comprised of 891.5 nm and 518.0 nm. At 0.1 G (Fig. 5a), the fidelity yielded at $x \neq x_0$ is suppressed. In this regime the quantization axis is poorly defined. Increasing the magnetic field to 1 G (Fig. 5b) shows the emergence of the perturbative regime signified by the broadening around β_0 of nonzero fidelity. However, at both edges of the figure (representing monochromatic potentials, fidelity remains suppressed). Finally, at 5 G (Fig. 5c), the quantization axis is better resolved, which we can quantify by the increase in the fidelity plateau region along β_0 as shown by the blue contour. In all scenarios, the region in the vicinity of x_0, β_0 , maintains a plateau of high fidelity. For both the low and the high magnetic field amplitude we observe the presence of this region. As the magnetic field is increased, the high fidelity plateau is broader with respect to x . Furthermore, the shape of the plateau highlights the trade-off between power and angle stability. However, we note that $5s5p$ 3P_2 has a significant quadratic Zeeman shift [63] that we calculate to be $\Delta_B^2 \approx (188.7 \text{ Hz}/G^2)m_F^2 B^2$ (see Appendix. D). Therefore, compensation of the quadratic Zeeman shift with the power ratio can only be achieved for a range of magnetic fields. We expect that operating at $\lesssim 5$ G would enable our light shift scheme to compensate for the quadratic Zeeman shift while preserving state fidelity.

Our analysis highlights the light shift engineering realized by bichromatic tweezers: it realizes a light shift regime in which the off-diagonal elements in Eq. (1) are small compared to the diagonal elements. This is the perturbative regime in which magic-angle tuning *can be engineered*, enabling the preservation of qudit coherence by suppressing dephasing induced by the trapping potential while operating at achievable angular precision and magnetic fields.

III. TWEEZER-INDUCED DECOHERENCE IN BICHROMATIC TWEEZERS

Optical tweezers (at frequency ω , see Fig. 6) induce via Rayleigh and Raman scattering that impact qudit coherence. Rayleigh scattering (see Fig. 6a) is an elastic process [25, 64] that does not change the atom's internal state and is characterized by scattered photons' maintaining frequency ω . However, for 3P_2 , this process yields differential scattering amplitudes between nuclear spins in ^{87}Sr , introducing a dephasing mechanism [27, 65]. In contrast, Raman scattering is an inelastic process (see Fig. 6a) characterized by a change of *color*, $\omega \rightarrow \omega_{sc}$, which changes the atom's internal state because of spontaneous optical pumping. This process leads to the emergence of depolarizing errors and leakage errors [66] (see Fig. 6b).

A. Leakage Errors

In this section we present the scattering rates for bichromatic tweezers. For both configurations presented in this work (813.5 nm - 521.3 nm and 891.5 nm - 518.0 nm) we set β to β_0 ; the respective trap depth are 164 μK and 144 μK respective; the $1/e^2$ beam waist radius is 1 micron for both configurations. Finally, we note that a tweezer using 891.5 nm and 518.0 nm, yields an effective 327 nm photon, below the ionization threshold.

In Table II and Table III we present the leakage errors within ${}^3\text{P}_2$ for the two configurations presented in this work. We calculate the scattering rates for bichromatic tweezers as follows: (1) we compute the individual scattering rates for each wavelength; (2) combine the rates to yield the total scattering rate; (3) take the average to yield the scattering rate process for a qudit in ${}^{87}\text{Sr}$. We note that for the case $F' = 9/2$ we look for depolarization channels in which the state undergoes $|F, m_F\rangle \rightarrow |F, m_{F'}\rangle$ where $m_F \neq m_{F'}$.

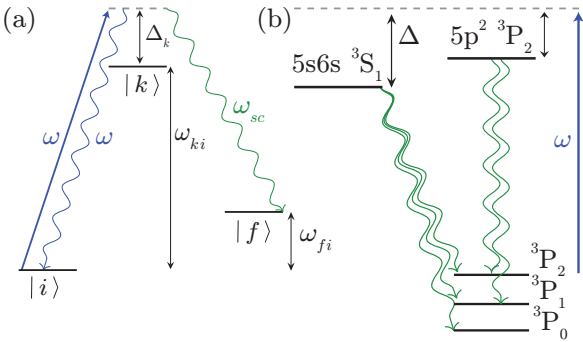


Figure 6. Tweezer-Induced Scattering Processes in ${}^3\text{P}_2$
 (a) Optical tweezers' far-detuned light is represented by the blue line (corresponding for ω) connecting a trapped qudit in the computational state $|i\rangle$ with dipole-allowed transitions to excited state $|k\rangle$, which introduce virtual states, detuned by Δ_k from $|k\rangle$ indicated by dashed gray lines. These states open decay (error) channels for qudits. When scattered photons (curly line) maintain frequency ω , this represents a Rayleigh scattering event. In contrast, a Raman scattering occurs when scattered photons change color (from blue to green) $\omega \rightarrow \omega_{sc}$. This process enables a qudit to decay to a different state $|f\rangle$.
 (b) Leakage Errors in ${}^3\text{P}_2$. In ${}^3\text{P}_2$, excited states presented in this figure create decay paths to other metastable states in ${}^{87}\text{Sr}$ such as ${}^3\text{P}_0$ and ${}^3\text{P}_1$ that a qudit can access by Raman scattering.

1. Blackbody Radiation-induced Optical Pumping

The blackbody spectrum at room temperature introduces an additional error channel: optical pumping induced by blackbody radiation (BBR) [67–70]. In $5s5p\ {}^3\text{P}_2$ this enables leakage to ${}^3\text{D}_J$ manifold. We can represent this error rate as a function of temperature,

$ {}^3\text{P}_2, F = 9/2\rangle \rightarrow {}^3\text{P}_2, F'\rangle$	Γ
$F' = 5/2$	0.020
$F' = 7/2$	0.025
$F' = 9/2$	0.018
$F' = 11/2$	0.044
$F' = 13/2$	0.015
$ {}^3\text{P}_2, F = 9/2\rangle \rightarrow {}^3\text{P}_J, F'\rangle$	Γ
${}^3\text{P}_1$	
$F' = 7/2$	0.079
$F' = 9/2$	0.137
$F' = 11/2$	0.049
${}^3\text{P}_0$	
$F' = 9/2$	0.066

Table II. Average Raman Scattering Rates within ${}^3\text{P}_2$ and to other metastable states ${}^3\text{P}_J$ in Bichromatic Tweezer at β_0 using 813.5 nm and 521.3 nm. Γ is in units of photons/sec.

$ {}^3\text{P}_2, F = 9/2\rangle \rightarrow {}^3\text{P}_2, F'\rangle$	Γ
$F' = 5/2$	0.014
$F' = 7/2$	0.018
$F' = 9/2$	0.012
$F' = 11/2$	0.031
$F' = 13/2$	0.011
$ {}^3\text{P}_2, F = 9/2\rangle \rightarrow {}^3\text{P}_J, F'\rangle$	Γ
${}^3\text{P}_1$	
$F' = 7/2$	0.068
$F' = 9/2$	0.133
$F' = 11/2$	0.039
${}^3\text{P}_0$	
$F' = 9/2$	0.057

Table III. Average Raman Scattering Rates within ${}^3\text{P}_2$ and to other metastable states ${}^3\text{P}_J$ in Bichromatic Tweezer at β_0 using 891.5 nm and 518.0 nm. Γ is in units of photons/sec.

$$\Gamma_{\text{BBR}, i \rightarrow f}(T) = \sum_k b_{i,k} b_{k,f} \frac{A_{ik}}{e^{\hbar\omega_{i,k}/k_B T} - 1}, \quad (11)$$

In Eq. (11), A_{ik} represents the Einstein A-coefficient $i \rightarrow k$, $\omega_{i,k}$ is the angular frequency between the two states of interest, $i \equiv \{S_i, L_i, J_i\}$ encodes the angular momentum degrees of freedom, and $b_{i,k}$ represent the branching ratios [64, 69, 71],

$$b_{i,k} = (2J_i + 1)(2L_k + 1) \left\{ \begin{array}{ccc} L_i & J_i & S_i \\ J_k & L_k & 1 \end{array} \right\}^2 \quad (12)$$

We are interested in estimating the leakage rate for $e \rightarrow k \rightarrow f$ error channel (where $k = 5s4d\ {}^3\text{D}_J$ and $f = {}^3\text{P}_1$). Using corresponding branching ratios [69] and the radiative decay rate [70, 72], this process yields a quenching rate of 8.03×10^{-3} photons/sec [70] at $T = 299.5\text{ K}$.

B. Photoionization in 3P_2 at 521.3 nm

The use of wavelengths in the vicinity of 521 nm comes with a drawback: the introduction a loss channel via two-photon photoionization in metastable states. The wavelengths required to photo-ionize in ${}^{87}\text{Sr}$ are 218 nm, 317 nm, 318 nm, and 322 nm for ${}^1\text{S}_0$, ${}^3\text{P}_0$, ${}^3\text{P}_1$ and ${}^3\text{P}_2$ respectively. Two photons with a combined effective energy above the ionization threshold allow for an ionization out of $5s5p\ {}^3\text{P}_J$ to the continuum [73]. This effect has been observed in 520 nm tweezers [8, 74, 75] for ${}^3\text{P}_0$ and ${}^3\text{P}_1$. For ${}^3\text{P}_2$ our bichromatic tweezers operating at 813.5 nm and 521.3 nm, wavelengths which yield an effective energy higher than the ionization threshold, introduce this loss mechanism.

For the purposes of benchmarking this process in our tweezer in ${}^3\text{P}_2$, we will extrapolate from the ionization rate in ${}^3\text{P}_0$ measured in F. Gyger et. al. [75], $250\text{ sec}^{-1}\text{ mK}^{-2}$. Furthermore, we will use this rate for our 521.3 nm tweezer. The trap depth contribution for 521.3 nm is $123\text{ }\mu\text{K}$, yielding a photoionization rate of 3.8 sec^{-1} . There is a second photoionization process combining a 813.5 nm photon and a 521.3 nm photon that will increase the photoionization rate, which we have not carefully considered. If this process yields a rate that becomes the limiting factor for our approach, it can be ameliorated by operating at different set of wavelengths, such as 891.5 nm and 518.0 nm, where only the shorter wavelength photons can combine to exceed the ionization threshold. See Table. III for the corresponding scattering rates for this configuration. Given our expected gate speeds, less than 1 ms, we do not expect these processes to be limiting factors for our scheme.

Other issues with tweezers in the vicinity of 521 nm have been identified as opening a loss channel on the ${}^1\text{P}_1 \rightarrow {}^1\text{D}_2$ decay that occurs when cycling ${}^1\text{S}_0 \rightarrow {}^1\text{P}_1$, essential for state detection in our scheme. This loss mechanism arises because ${}^1\text{D}_2$ is anti trapped near the vicinity of 515 nm; see Fig. A.2 in Appendix A 2. In contrast, for our scheme at 521.3 nm (and 518.0 nm), ${}^1\text{D}_2$ is trapped, mitigating this loss channel.

C. Rayleigh Decoherence in 3P_2

Unlike ${}^3\text{P}_0$, the presence of resolvable hyperfine structure in ${}^3\text{P}_2$ allows for differential scattering amplitudes between nuclear spins, leading to Rayleigh-induced decoherence [26, 76]. For qubits this effect is represented by a sole figure of merit: differential scattering amplitude between two nuclear spins comprising a qubit; e.g. a hyperfine qubit $\frac{1}{\sqrt{2}}(|0\rangle + |1\rangle)$ in Yb [27]. In contrast, qudits' symmetry structure require a modification to the result in H. Uys et. al. [26]. We define an effective Rayleigh scattering for each nuclear spin in the hyperfine manifold using Eq. (E26) in Appendix E. We will calculate this figure of merit to estimate impact on qudit coherence.

We present the results of this calculation in Table. IV for the two configurations presented in this paper. The

effective Rayleigh rates are computed as follows: (1) we calculate the given difference in Rayleigh scattering between a given $i \equiv |F, m_F\rangle$ hyperfine state in the qudit (e.g $m_F = 9/2$) and $j \equiv |F, m_{F'}\rangle$ nuclear spin in the qudit; (2) exhaustively go through all remaining j nuclear spins in the manifold (e.g $m'_F = 7/2, \dots, -9/2$); (3) take the average.

813.5 nm and 521.3 nm		
m_F	$\Gamma_{\text{Scattering}}$	$\Gamma_{\text{Decoherence}}$
$\pm 9/2$	3.906	0.064
$\pm 7/2$	3.871	0.029
$\pm 5/2$	3.864	0.023
$\pm 3/2$	3.869	0.028
$\pm 1/2$	3.875	0.033

891.5 nm and 518.0 nm		
m_F	$\Gamma_{\text{Scattering}}$	$\Gamma_{\text{Decoherence}}$
$\pm 9/2$	3.705	0.045
$\pm 7/2$	3.681	0.020
$\pm 5/2$	3.676	0.016
$\pm 3/2$	3.679	0.019
$\pm 1/2$	3.683	0.023

Table IV. Comparison of traditional Rayleigh scattering and decoherence error rates in Bichromatic Tweezers for ${}^3\text{P}_2$ $F = 9/2$ at β_0 . All Γ values are in units of photons/sec.

By operating at the magic angle β_0 , the bichromatic approach enables the mitigation of Rayleigh decoherence. In Table. IV we estimate both Rayleigh scattering and decoherence rates. At β_0 , $d_{\pm 1}$ contributions need to be considered in the scattering calculation (see Appendix. E 1 b) in addition to d_0 contributions.

IV. CONCLUSION

We have shown the viability of engineering magic trapping conditions for all m_F in $5s5p\ {}^3\text{P}_2$ $F = 9/2$ of ${}^{87}\text{Sr}$ via bichromatic tweezers by carefully choosing a power ratio between two wavelengths and magic-angle tuning to the tensor magic angle. We apply this technique to engineer magic trapping conditions in ${}^1\text{S}_0 - {}^3\text{P}_2$ with two configurations: (1) employing two scalar magic wavelengths at 891.5 nm and 518.0 nm, and (2) using the ${}^1\text{S}_0 - {}^3\text{P}_0$ magic wavelength at 813.5 nm and an additional wavelength at 521.3 nm.

We determine that for a high-spin hyperfine manifold a monochromatic tweezer is incompatible with magic-angle tuning: this technique requires magnetic fields well within the Paschen-Back regime (where $|F, m_F\rangle$ is no longer a good quantum basis) to define the quantization axis. Our work suggests that operating at a magnetic field of $\lesssim 5\text{ G}$ would enable suppression of tweezer-induced dephasing with our scheme while also mitigating the impact of the quadratic Zeeman shift [63] on qudit fidelity. Furthermore, since our light shift cancellation relies on scaling *down*

the light shift Hamiltonian rather than scaling *up* the bias magnetic field, the perturbative regime needed for magic-angle tuning can be enforced at low magnetic fields. These conditions enable operating at the magic angle at practical angular precision, leading to the suppression of light shift induced-dephasing and Rayleigh decoherence — key ingredients in preserving qudit coherence. We expect the bichromatic tweezer to enhance state fidelity, and enable the assembly of atomic arrays ideal for qudit-based quantum sensing, simulation, and computing applications in ^{87}Sr .

We thank K. Gan, B. Madhusudhana and S. Alperin for advising on considerations regarding the viability of this

scheme throughout this project; M. Safronova for providing reduced dipole matrix elements for $^1\text{S}_0$ and $5s4d\ ^1\text{D}_2$; B. Hunt, S. Pampel, Y. Liu, T. Hoang, and E. Gurra for meaningful conversations during the preparation of this manuscript.

This work was supported by the Laboratory Directed Research and Development program of Los Alamos National Laboratory under project numbers 20210116DR, 20210955PRD3, and 20240295ER, the NSF Quantum Leap Challenge Institutes program, Award No. 2016244, and presented at the Aspen Center for Physics, which is supported by National Science Foundation grant PHY-2210452.

[1] A. Kaufman and K.-K. Ni, Quantum science with optical tweezer arrays of ultracold atoms and molecules, *Nature Physics* **10**, 1038/s41567-021-01357-2 (2021).

[2] K. Barnes, P. Battaglino, B. J. Bloom, K. Cassella, R. Coxe, N. Crisosto, J. P. King, S. S. Kondov, K. Kotru, S. C. Larsen, J. Lauigan, B. J. Lester, M. McDonald, E. Megidish, S. Narayanaswami, C. Nishiguchi, R. Notermans, L. S. Peng, A. Ryou, T.-Y. Wu, and M. Yarwood, Assembly and coherent control of a register of nuclear spin qubits, *Nature Communications* **13**, 10.1038/s41467-022-29977-z (2022).

[3] T. Ido and H. Katori, Recoil-free spectroscopy of neutral sr atoms in the lamb-dicke regime, *Phys. Rev. Lett.* **91**, 053001 (2003).

[4] R. Yamamoto, J. Kobayashi, T. Kuno, K. Kato, and Y. Takahashi, An ytterbium quantum gas microscope with narrow-line laser cooling, *New Journal of Physics* **18**, 023016 (2016).

[5] A. Aeppli, K. Kim, W. Warfield, M. S. Safronova, and J. Ye, Clock with 8×10^{-19} systematic uncertainty, *Phys. Rev. Lett.* **133**, 023401 (2024).

[6] R. Santra, E. Arimondo, T. Ido, C. H. Greene, and J. Ye, High-accuracy optical clock via three-level coherence in neutral bosonic ^{88}Sr , *Phys. Rev. Lett.* **94**, 173002 (2005).

[7] V. Klüsener, S. Pucher, D. Yankelev, J. Trautmann, F. Spietersbach, D. Filin, S. G. Porsev, M. S. Safronova, I. Bloch, and S. Blatt, Long-lived coherence on a μHz scale optical magnetic quadrupole transition, *Phys. Rev. Lett.* **132**, 253201 (2024).

[8] A. Cooper, J. P. Covey, I. S. Madjarov, S. G. Porsev, M. S. Safronova, and M. Endres, Alkaline-earth atoms in optical tweezers, *Phys. Rev. X* **8**, 041055 (2018).

[9] H. Katori, T. Ido, Y. Isoya, and M. Kuwata-Gonokami, Magneto-optical trapping and cooling of strontium atoms down to the photon recoil temperature, *Phys. Rev. Lett.* **82**, 1116 (1999).

[10] S. Saskin, J. T. Wilson, B. Grinkemeyer, and J. D. Thompson, Narrow-line cooling and imaging of ytterbium atoms in an optical tweezer array, *Phys. Rev. Lett.* **122**, 143002 (2019).

[11] A. Urech, I. H. A. Knottnerus, R. J. C. Spreeuw, and F. Schreck, Narrow-line imaging of single strontium atoms in shallow optical tweezers, *Phys. Rev. Res.* **4**, 023245 (2022).

[12] C.-C. Chen, J. L. Siegel, B. D. Hunt, T. Grogan, Y. S. Hassan, K. Beloy, K. Gibble, R. C. Brown, and A. D. Ludlow, Clock-line-mediated sisyphus cooling, *Phys. Rev. Lett.* **133**, 053401 (2024).

[13] A. V. Gorshkov, M. Hermele, V. Gurarie, C. Xu, P. S. Julienne, J. Ye, P. Zoller, E. Demler, M. D. Lukin, and A. M. Rey, Two-orbital $s\ u(n)$ magnetism with ultracold alkaline-earth atoms, *Nature Physics* **6**, 289–295 (2010).

[14] S. Omanakuttan, A. Mitra, M. J. Martin, and I. H. Deutsch, Quantum optimal control of ten-level nuclear spin qudits in ^{87}Sr , *Phys. Rev. A* **104**, L060401 (2021).

[15] A. J. Daley, J. Ye, and P. Zoller, State-dependent lattices for quantum computing with alkaline-earth-metal atoms, *The European Physical Journal D* **65**, 207–217 (2011).

[16] Y. A. Yang, W.-T. Luo, J.-L. Zhang, S.-Z. Wang, C.-L. Zou, T. Xia, and Z.-T. Lu, Minute-scale schrödinger-cat state of spin-5/2 atoms, *Nature Photonics* **19**, 89–94 (2024).

[17] S. Omanakuttan, V. Buchemavari, J. A. Gross, I. H. Deutsch, and M. Marvian, Fault-tolerant quantum computation using large spin-cat codes, *PRX Quantum* **5**, 020355 (2024).

[18] H. J. Manetsch, G. Nomura, E. Bataille, K. H. Leung, X. Lv, and M. Endres, A tweezer array with 6100 highly coherent atomic qubits (2024), arXiv:2403.12021 [quant-ph].

[19] A. W. Young, W. J. Eckner, W. R. Milner, D. Kedar, M. A. Norcia, E. Oelker, N. Schine, J. Ye, and A. M. Kaufman, Half-minute-scale atomic coherence and high relative stability in a tweezer clock, *Nature* **588**, 408–413 (2020).

[20] I. S. Madjarov, A. Cooper, A. L. Shaw, J. P. Covey, V. Schkolnik, T. H. Yoon, J. R. Williams, and M. Endres, An atomic-array optical clock with single-atom readout, *Phys. Rev. X* **9**, 041052 (2019).

[21] J. P. Covey, I. S. Madjarov, A. Cooper, and M. Endres, 2000-times repeated imaging of strontium atoms in clock-magic tweezer arrays, *Phys. Rev. Lett.* **122**, 173201 (2019).

[22] A. Cao, W. J. Eckner, T. Lukin Yelin, A. W. Young, S. Jandura, L. Yan, K. Kim, G. Pupillo, J. Ye, N. Darkwah Oppong, and A. M. Kaufman, Multi-qubit gates and schrödinger cat states in an optical clock, *Nature* **634**, 315–320 (2024).

[23] R. Finkelstein, R. B.-S. Tsai, X. Sun, P. Scholl, S. Direkci, T. Gefen, J. Choi, A. L. Shaw, and M. Endres, Universal

quantum operations and ancilla-based read-out for tweezer clocks, *Nature* **634**, 321–327 (2024).

[24] S. Kuhr, W. Alt, D. Schrader, I. Dotsenko, Y. Miroshnychenko, A. Rauschenbeutel, and D. Meschede, Analysis of dephasing mechanisms in a standing-wave dipole trap, *Phys. Rev. A* **72**, 023406 (2005).

[25] S. Dörscher, R. Schwarz, A. Al-Masoudi, S. Falke, U. Sterr, and C. Lisdat, Lattice-induced photon scattering in an optical lattice clock, *Phys. Rev. A* **97**, 063419 (2018).

[26] H. Uys, M. J. Biercuk, A. P. VanDevender, C. Ospelkaus, D. Meiser, R. Ozeri, and J. J. Bollinger, Decoherence due to elastic rayleigh scattering, *Phys. Rev. Lett.* **105**, 200401 (2010).

[27] A. Jenkins, J. W. Lis, A. Senoo, W. F. McGrew, and A. M. Kaufman, Ytterbium nuclear-spin qubits in an optical tweezer array, *Phys. Rev. X* **12**, 021027 (2022).

[28] S. Omanakuttan, A. Mitra, E. J. Meier, M. J. Martin, and I. H. Deutsch, Qudit entanglers using quantum optimal control, *PRX Quantum* **4**, 040333 (2023).

[29] I. Reichenbach and I. H. Deutsch, Sideband cooling while preserving coherences in the nuclear spin state in group-ii-like atoms, *Phys. Rev. Lett.* **99**, 123001 (2007).

[30] X.-F. Shi, Coherence-preserving cooling of nuclear-spin qubits in a weak magnetic field, *Phys. Rev. A* **107**, 023102 (2023).

[31] S. Omanakuttan, V. Buchemavari, M. J. Martin, and I. H. Deutsch, *Coherence preserving leakage detection and cooling in alkaline earth atoms* (2024), arXiv:2410.23430 [quant-ph].

[32] S. Stellmer, R. Grimm, and F. Schreck, Detection and manipulation of nuclear spin states in fermionic strontium, *Phys. Rev. A* **84**, 043611 (2011).

[33] T. O. Höhn, E. Staub, G. Brochier, N. Darkwah Oppong, and M. Aiedsburger, State-dependent potentials for the 1s_0 and 3p_0 clock states of neutral ytterbium atoms, *Phys. Rev. A* **108**, 053325 (2023).

[34] F. Le Kien, P. Schneeweiss, and A. Rauschenbeutel, Dynamical polarizability of atoms in arbitrary light fields: general theory and application to cesium, *The European Physical Journal D* **67**, 10.1140/epjd/e2013-30729-x (2013).

[35] M. A. Norcia, A. W. Young, and A. M. Kaufman, Microscopic control and detection of ultracold strontium in optical-tweezer arrays, *Phys. Rev. X* **8**, 041054 (2018).

[36] M. A. Norcia, A. W. Young, W. J. Eckner, E. Oelker, J. Ye, and A. M. Kaufman, Seconds-scale coherence on an optical clock transition in a tweezer array, *Science* **366**, 93–97 (2019).

[37] R. Journet, F. Faisant, S. Lee, and M. Cheneau, Differential polarizability of the strontium intercombination transition at 1064.7 nm, *Phys. Rev. A* **110**, 032819 (2024).

[38] T. O. Höhn, R. A. Villela, E. Zu, L. Bezzo, R. M. Kroese, and M. Aiedsburger, Determining the 3p_0 excited-state tune-out wavelength of ^{174}yb in a triple-magic lattice (2024), arXiv:2412.14163 [cond-mat.quant-gas].

[39] J. W. Lis, A. Senoo, W. F. McGrew, F. Rönchen, A. Jenkins, and A. M. Kaufman, Midcircuit operations using the omg architecture in neutral atom arrays, *Phys. Rev. X* **13**, 041035 (2023).

[40] V. D. Ovsiannikov, V. G. Pal'chikov, A. V. Taichenachev, V. I. Yudin, and H. Katori, Multipole, nonlinear, and anharmonic uncertainties of clocks of sr atoms in an optical lattice, *Phys. Rev. A* **88**, 013405 (2013).

[41] T. Bothwell, *A Wannier-Stark Optical Lattice Clock With Extended Coherence Times*, Ph.D. thesis, University of Colorado Boulder (2022).

[42] M. V. Romalis and E. N. Fortson, Zeeman frequency shifts in an optical dipole trap used to search for an electric-dipole moment, *Phys. Rev. A* **59**, 4547 (1999).

[43] M. Mazzanti, R. X. Schüssler, J. D. Arias Espinoza, Z. Wu, R. Gerritsma, and A. Safavi-Naini, Trapped ion quantum computing using optical tweezers and electric fields, *Phys. Rev. Lett.* **127**, 260502 (2021).

[44] J. Schmidt, P. Weckesser, F. Thielemann, T. Schaetz, and L. Karpa, Optical traps for sympathetic cooling of ions with ultracold neutral atoms, *Phys. Rev. Lett.* **124**, 053402 (2020).

[45] F. Le Kien, V. I. Balykin, and K. Hakuta, Atom trap and waveguide using a two-color evanescent light field around a subwavelength-diameter optical fiber, *Phys. Rev. A* **70**, 063403 (2004).

[46] A. Hilton, C. Perrella, A. Luiten, and P. Light, Dual-color magic-wavelength trap for suppression of light shifts in atoms, *Phys. Rev. Appl.* **11**, 024065 (2019).

[47] V. Gerginov and K. Beloy, Two-photon optical frequency reference with active ac stark shift cancellation, *Phys. Rev. Appl.* **10**, 014031 (2018).

[48] J. S. Rosenberg, L. Christakis, E. Guardado-Sánchez, Z. Z. Yan, and W. S. Bakr, Observation of the hanbury brown–twiss effect with ultracold molecules, *Nature Physics* **18**, 1062–1066 (2022).

[49] A. Ciamei, S. Finelli, A. Cosco, M. Inguscio, A. Trenkwalder, and M. Zaccanti, Double-degenerate fermi mixtures of ^6Li and ^{53}Cr atoms, *Phys. Rev. A* **106**, 053318 (2022).

[50] K. E. Wilson, A. Guttridge, J. Segal, and S. L. Cornish, Quantum degenerate mixtures of cs and yb, *Phys. Rev. A* **103**, 033306 (2021).

[51] A. Wallucks, I. Marinković, B. Hensen, R. Stockill, and S. Gröblacher, A quantum memory at telecom wavelengths, *Nature Physics* **16**, 772–777 (2020).

[52] A. W. Carr and M. Saffman, Doubly magic optical trapping for cs atom hyperfine clock transitions, *Phys. Rev. Lett.* **117**, 150801 (2016).

[53] A. Kaplan, M. Fredslund Andersen, and N. Davidson, Suppression of inhomogeneous broadening in rf spectroscopy of optically trapped atoms, *Phys. Rev. A* **66**, 045401 (2002).

[54] S. Jackson and A. C. Vutha, Magic polarization for cancellation of light shifts in two-photon optical clocks, *Phys. Rev. A* **99**, 063422 (2019).

[55] S. J. Masson, Z. Yan, J. Ho, Y.-H. Lu, D. M. Stamper-Kurn, and A. Asenjo-Garcia, State-insensitive wavelengths for light shifts and photon scattering from zeeman states, *Phys. Rev. A* **109**, 063105 (2024).

[56] J. Ye, H. J. Kimble, and H. Katori, Quantum state engineering and precision metrology using state-insensitive light traps, *Science* **320**, 1734 (2008).

[57] D. Burba, H. Dunikowski, M. Robert-de Saint-Vincent, E. Witkowska, and G. Juzeliūnas, Effective light-induced hamiltonian for atoms with large nuclear spin, *Phys. Rev. Res.* **6**, 033293 (2024).

[58] C. Shi, J.-L. Robyr, U. Eismann, M. Zawada, L. Lorini, R. Le Targat, and J. Lodewyck, Polarizabilities of the ^{87}Sr clock transition, *Phys. Rev. A* **92**, 012516 (2015).

[59] J. Trautmann, D. Yankelev, V. Klüsener, A. J. Park, I. Bloch, and S. Blatt, $^1\text{S}_0 - ^3\text{P}_2$ magnetic quadrupole transition in neutral strontium, *Phys. Rev. Res.* **5**, 013219

(2023).

[60] J. Ye, H. J. Kimble, and H. Katori, Quantum state engineering and precision metrology using state-insensitive light traps, *Science* **320**, 1734–1738 (2008).

[61] T. Volkoff, Z. Holmes, and A. Sornborger, Universal compiling and (no-)free-lunch theorems for continuous-variable quantum learning, *PRX Quantum* **2**, 040327 (2021).

[62] L. H. Pedersen, N. M. Møller, and K. Mølmer, Fidelity of quantum operations, *Physics Letters A* **367**, 47–51 (2007).

[63] M. M. Boyd, T. Zelevinsky, A. D. Ludlow, S. Blatt, T. Zanon-Willette, S. M. Foreman, and J. Ye, Nuclear spin effects in optical lattice clocks, *Physical Review A* **76**, 10.1103/physreva.76.022510 (2007).

[64] M. J. Martin, *Quantum Metrology and Many-Body Physics: Pushing the Frontier of the Optical Lattice Clock*, Ph.D. thesis, University of Colorado Boulder (2013).

[65] H. Uys, M. J. Biercuk, A. P. VanDevender, C. Ospelkaus, D. Meiser, R. Ozeri, and J. J. Bollinger, Decoherence due to elastic rayleigh scattering, *Phys. Rev. Lett.* **105**, 200401 (2010).

[66] P. Scholl, A. L. Shaw, R. B.-S. Tsai, R. Finkelstein, J. Choi, and M. Endres, Erasure conversion in a high-fidelity rydberg quantum simulator, *Nature* **622**, 273–278 (2023).

[67] C. Lisdat, S. Dörscher, I. Nosske, and U. Sterr, Blackbody radiation shift in strontium lattice clocks revisited, *Phys. Rev. Res.* **3**, L042036 (2021).

[68] J. R. Guest, N. D. Scielzo, I. Ahmad, K. Bailey, J. P. Greene, R. J. Holt, Z.-T. Lu, T. P. O'Connor, and D. H. Potterveld, Laser trapping of ^{225}Ra and ^{226}Ra with repumping by room-temperature blackbody radiation, *Phys. Rev. Lett.* **98**, 093001 (2007).

[69] I. R. Hill, *Development of an apparatus for a strontium optical lattice optical frequency standard*, Ph.D. thesis, Imperial College London (2012).

[70] M. Yasuda and H. Katori, Lifetime measurement of the 3p_2 metastable state of strontium atoms, *Phys. Rev. Lett.* **92**, 153004 (2004).

[71] A. Ludlow, *The Strontium Optical Lattice Clock: Optical Spectroscopy with Sub-Hertz Accuracy*, Ph.D. thesis, Boulder (2008).

[72] M. S. Safranova, S. G. Porsev, U. I. Safranova, M. G. Kozlov, and C. W. Clark, Blackbody-radiation shift in the sr optical atomic clock, *Phys. Rev. A* **87**, 012509 (2013).

[73] A. Young, *Programmable arrays of alkaline earth atoms: qubits, clocks, and the Bose-Hubbard model*, Ph.D. thesis, University of Colorado Boulder (2023).

[74] A. Holman, Y. Xu, X. Sun, J. Wu, M. Wang, B. Seo, N. Yu, and S. Will, *Trapping of single atoms in meta-surface optical tweezer arrays* (2024), arXiv:2411.05321 [physics.atom-ph].

[75] F. Gyger, M. Ammenwerth, R. Tao, H. Timme, S. Snigirev, I. Bloch, and J. Zeiher, *Continuous operation of large-scale atom arrays in optical lattices* (2024), arXiv:2402.04994 [quant-ph].

[76] I. D. Moore, *Easy on the Ions: Photon Scattering Errors from Far-Detuned Raman Beams in Trapped-Ion Qubits*, Ph.D. thesis (2023).

[77] F. Le Kien, P. Schneeweiss, and A. Rauschenbeutel, Dynamical polarizability of atoms in arbitrary light fields: general theory and application to cesium, *The European Physical Journal D* **67**, 10.1140/epjd/e2013-30729-x (2013).

[78] D. Steck, *Quantum and Atom Optics* (2024).

[79] I. S. Madjarov, *Entangling, Controlling, and Detecting Individual Strontium Atoms in Optical Tweezer Arrays*, Ph.D. thesis, California Institute of Technology (2021).

[80] D. Budker, D. Kimball, and D. DeMille, *Atomic physics: An exploration through problems and solutions* (OUP Oxford, 2008).

[81] M. Auzinsh, D. Budker, and S. Rochester, *Optically Polarized Atoms: Understanding Light-atom Interactions* (OUP Oxford, 2010).

[82] B. E. King, *Angular momentum coupling and rabi frequencies for simple atomic transitions* (2008), arXiv:0804.4528 [physics.atom-ph].

[83] M. S. Safranova, (private communication).

[84] J. Trautmann, *The magnetic quadrupole transition in neutral strontium*, Ph.D. thesis, Munich U. (2022).

[85] A. Kramida, Yu. Ralchenko, J. Reader, and and NIST ASD Team, NIST Atomic Spectra Database (ver. 5.12), [Online]. Available: <https://physics.nist.gov/asd> [2017, April 9]. National Institute of Standards and Technology, Gaithersburg, MD. (2024).

[86] G. Unnikrishnan, P. Ilzhöfer, A. Scholz, C. Hözl, A. Götzelmänn, R. K. Gupta, J. Zhao, J. Krauter, S. Weber, N. Makki, H. P. Büchler, T. Pfau, and F. Meinert, Coherent control of the fine-structure qubit in a single alkaline-earth atom, *Phys. Rev. Lett.* **132**, 150606 (2024).

[87] M. Ammenwerth, H. Timme, F. Gyger, R. Tao, I. Bloch, and J. Zeiher, *Realization of a fast triple-magic all-optical qutrit in strontium-88* (2024), arXiv:2411.02869 [physics.atom-ph].

[88] J. D. Thompson, T. G. Tiecke, A. S. Zibrov, V. Vuletić, and M. D. Lukin, Coherence and raman sideband cooling of a single atom in an optical tweezer, *Phys. Rev. Lett.* **110**, 133001 (2013).

[89] A. Kaufman, *Laser cooling atoms to indistinguishability: Atomic Hong-Ou-Mandel interference and entanglement through spin exchange*, Ph.D. thesis, Boulder, CO (2015).

[90] L. Novotny and B. Hecht, *Principles of Nano-Optics* (Cambridge University Press, 2006).

[91] D. Bluvstein, H. Levine, G. Semeghini, T. T. Wang, S. Ebadi, M. Kalinowski, A. Keesling, N. Maskara, H. Pichler, M. Greiner, V. Vuletić, and M. D. Lukin, A quantum processor based on coherent transport of entangled atom arrays, *Nature* **604**, 451–456 (2022).

[92] S. M. Heider and G. O. Brink, Hyperfine structure of ^{87}Sr in the 3p_2 metastable state, *Phys. Rev. A* **16**, 1371 (1977).

[93] P. Thekkepatt, Digvijay, A. Urech, F. Schreck, and K. van Druten, Measurement of the g factor of ground-state ^{87}Sr at the parts-per-million level using co-trapped ultracold atoms, *Phys. Rev. Lett.* **135**, 193001 (2025).

[94] A. Lurio, M. Mandel, and R. Novick, Second-order hyperfine and zeeman corrections for an (sl) configuration, *Phys. Rev.* **126**, 1758 (1962).

[95] L. Rieger, *Interorbital spin exchange in a state-dependent optical lattice* (2019).

[96] J. Walraven, *Atomic Physics, lecture notes* (2023).

Appendix A: Hyperfine Polarizability in ^{87}Sr

In this section we present the formalism used to estimate the atomic polarizabilities [77–79] for ^{87}Sr used in this

paper to find the appropriate wavelengths for light shift cancellation. In this paper computed the scalar, vector, and tensor bare hyperfine polarizabilities using following expressions,

$$\alpha_i^s(\omega) = \frac{2}{3\hbar} \frac{1}{(2F+1)} \sum_{n'F'} \langle nF' | \mathbf{d} | nF \rangle |^2 \frac{\omega_{n'F'nF}}{\omega_{n'F'nF}^2 - \omega^2} \quad (\text{A1})$$

$$\alpha_i^v(\omega) = \frac{1}{\hbar} \sum_{n'F'} \sqrt{\frac{24F}{(F+1)(2F+1)}} (-1)^{F'+F+1} \left\{ \begin{matrix} 1 & 1 & 1 \\ F & F' & F \end{matrix} \right\} \langle nF' | \mathbf{d} | nF \rangle |^2 \frac{\omega}{\omega_{n'F'nF}^2 - \omega^2} \quad (\text{A2})$$

$$\alpha_i^t(\omega) = \frac{1}{\hbar} \sqrt{\frac{40F(2F-1)}{3(F+1)(2F+1)(2F+3)}} \sum_{n'F'} (-1)^{F'+F} \left\{ \begin{matrix} 1 & 2 & 1 \\ F & F' & F \end{matrix} \right\} \langle nF' | \mathbf{d} | nF \rangle |^2 \frac{\omega_{n'F'nF}}{\omega_{n'F'nF}^2 - \omega^2} \quad (\text{A3})$$

$\omega_{n'F'nF}$ represents frequency detunings for each of the k excited states for a given electronic state. Furthermore,

$\langle nF' | \mathbf{d} | nF \rangle$ represent hyperfine structure reduced matrix elements (RDMEs), which can be computed from known $\langle nJ' | \mathbf{d} | nJ \rangle$ (see Tables A.1 to A.3) via [80–82],

$$\langle n'J'I F' | \mathbf{d} | nJIF \rangle = (-1)^{J'+I+F+1} \sqrt{(2F+1)(2F'+1)} \left\{ \begin{matrix} F' & 1 & F \\ J & I & J' \end{matrix} \right\} \langle nJ' | \mathbf{d} | nJ \rangle$$

1. Negative Sign of Tensor Light Shift

Our light shift cancellation scheme is predicated on finding two wavelengths with comparable scalar polarizability (for yielding an isotropic trapping potential) and with opposite and comparable tensor polarizability (enabling the suppression of spin-dependent tensor light shifts). In this section we will illustrate the atomic structure conditions that enable us to estimate suitable wavelengths in ^{87}Sr .

In Eq. (A3) we can look closely at the bare tensor polarizability and isolate the angular momentum-specific term which depends on each dipole-allowed excited state transition summed over to yield the total tensor polarizability for a given wavelength,

$$\begin{aligned} & (-1)^{F'+F} \left\{ \begin{matrix} 1 & 2 & 1 \\ F & F' & F \end{matrix} \right\} \\ & = (-1)^{-F+F'} \frac{\sqrt{\frac{2}{15}} \sqrt{\frac{\Gamma(2F+4)}{\Gamma(2F-1)}}}{(F+F')(F+F'+1)(F+F'+2)} \\ & \quad \times \frac{1}{\Gamma(F-F'+2)\Gamma(-F+F'+2)} \end{aligned} \quad (\text{A4})$$

In Eq. (A4) we note that by construction Γ functions will yield positive values, leaving $(-1)^{F'-F}$ as a term that changes tensor sign for a given excited state $|n'F'\rangle$. Let

us define this phase term as $(-1)^{\Delta F}$ where $F' - F = \Delta F$. Now we take a closer look at the detuning contribution in the tensor polarizability,

$$\frac{\omega_{n'F'nF}}{\omega_{n'F'nF}^2 - \omega^2} \quad (\text{A5})$$

Eq. (A5) introduces another factor in determining the tensor polarizability sign for a given frequency by $(\omega_{n'F'nF} - \omega)$. Finally, let us consider the reduced dipole matrix element (RDME) presented in Eq. (A). This term introduce a phase term dependent on the specific hyperfine state accounted for in the light shift calculation. As each excited hyperfine state $|n'F'\rangle$ yields a different phase factor, the overall tensor sign for a given electronic state is weighted by the RDME of a given hyperfine state, which in effect enhances the tensor sign in the calculation.

In Fig. A.1 we present the breakdown of tensor light shift contribution for 813.5 nm and 521.3 nm. In the case of 813.5 nm $^3\text{P}_2$ the excited state with the most impact for determining its tensor polarizability sign (and magnitude) is $5s6p\ ^3\text{S}_1$ - as every other state is too far-detuned from 813.5 nm to yield a meaningful impact on overall tensor sign. In contrast, for 521.3 nm there are more excited states that impact the tensor light shift. In this case $5p^2\ ^3\text{P}_2$ has the largest RDME (see Table. A.3) which dominates the overall tensor light.

Table A.1. Relevant Wavelength and RDMEs for the Excited Manifold for ${}^1\text{S}_0$ and ${}^3\text{P}_0$.

State k	ΔE_{ki} (1/cm)	$\langle k D i \rangle$ (a.u.)
State $i = {}^1\text{S}_0$		
$5s5p {}^3\text{P}_1$	14504.3380	0.1508 [83]
$5s6p {}^3\text{P}_1$	33868.0000	0.0340 [83]
$5s5p {}^1\text{P}_1$	21698.4520	5.2479 [83]
$5s6p {}^1\text{P}_1$	34098.4040	0.2664 [83]
$5s7p {}^1\text{P}_1$	38906.8580	0.3650 [83]
$5s8p {}^1\text{P}_1$	42462.1360	0.5900 [5]
$5s9p {}^1\text{P}_1$	43328.0400	0.4575 [5]
$5s10p {}^1\text{P}_1$	43938.2010	0.3394 [5]
$5s11p {}^1\text{P}_1$	44366.4200	0.2505 [5]
$5s12p {}^1\text{P}_1$	44675.7370	0.1996 [5]
$5s13p {}^1\text{P}_1$	44903.5000	0.1602 [5]
$5s14p {}^1\text{P}_1$	45075.2900	0.1375 [5]
$5s15p {}^1\text{P}_1$	45207.8300	0.1167 [5]
$4d5p {}^1\text{P}_1$	41172.0540	0.6005 [5]
Rydberg ${}^1\text{P}_1$	45932.2036	0.7037 [5]
State $i = {}^3\text{P}_0$		
$5s6s {}^3\text{S}_1$	14721.2660	1.9718 [5]
$5s7s {}^3\text{S}_1$	23107.1680	0.6099 [5]
$5s8s {}^3\text{S}_1$	26443.8650	0.2735 [5]
$5s9s {}^3\text{S}_1$	28133.6530	0.1849 [5]
$5s10s {}^3\text{S}_1$	29109.9330	0.1373 [5]
$5p^2 {}^3\text{P}_1$	21082.5980	2.4824 [5]
$4d^2 {}^3\text{P}_1$	30278.4130	1.6216 [5]
$5s4d {}^3\text{D}_1$	3841.5330	2.6906 [5]
$5s5d {}^3\text{D}_1$	20689.4010	2.7249 [5]
$5s6d {}^3\text{D}_1$	25368.3230	1.1388 [5]
$5s7d {}^3\text{D}_1$	27546.8470	0.7537 [5]
$5s8d {}^3\text{D}_1$	28749.1930	0.5475 [5]
$5s9d {}^3\text{D}_1$	29487.3830	0.4238 [5]
Rydberg ${}^3\text{S}_1$	31614.6966	0.2904 [5]
Rydberg ${}^3\text{D}_1$	31614.6966	0.4247 [5]

2. Light Shifts for $5s4d {}^1\text{D}_2$ near 521 nm

In this section we present the light shift calculations near 521 nm for $5s4d {}^1\text{D}_2$ as this is a potential atom loss channel when operating imaging via broad-line cooling in ${}^{87}\text{Sr}$.

In Fig. A.2 we present the results for linearly polarized light. We present all nuclear spins in $F = 9/2$ for $5s4d {}^1\text{D}_2$. At our chosen wavelength our trapping potential is trapping, mitigating atomic loss during imaging [79] experienced at 515 nm due to $5s4d {}^1\text{D}_2 \rightarrow 5s4f {}^1\text{F}_3$. Moreover, an atom in this state will experience a trapping potential at 813 nm as well.

3. Polarization Gradient-Induced Dephasing

High numerical-aperture objectives [86–89] create spatial-dependent polarization gradients that introduce

Table A.2. Relevant Wavelength and RDMEs for the Excited Manifold for ${}^3\text{P}_1$. $\alpha_c, \alpha_o = 5.6, 42.2$ a.u. taken from Trautmann Thesis [84].

State k	ΔE_{ki} (1/cm)	$\langle k D i \rangle$ (a.u.)
$5s^2 {}^1\text{S}_0$	-14505.000	0.151 [8]
$5s4d {}^3\text{D}_1$	3655.000	2.322 [8]
$5s4d {}^3\text{D}_2$	3714.000	4.019 [8]
$5s4d {}^1\text{D}_2$	5645.000	0.190 [8]
$5s6s {}^3\text{S}_1$	14534.000	3.425 [8]
$5s6s {}^1\text{S}_0$	16087.000	0.045 [8]
$5s5d {}^1\text{D}_2$	20223.000	0.061 [8]
$5s5d {}^3\text{D}_1$	20503.000	2.009 [8]
$5s5d {}^3\text{D}_2$	20518.000	3.673 [8]
$5p^2 {}^3\text{P}_0$	20689.000	2.657 [8]
$5p^2 {}^3\text{P}_1$	20896.000	2.362 [8]
$5p^2 {}^3\text{P}_2$	21170.000	2.865 [8]
$5p^2 {}^1\text{D}_2$	22457.000	0.228 [8]
$5p^2 {}^1\text{S}_0$	22656.000	0.291 [8]
$5s7s {}^3\text{S}_1$	22920.000	0.921 [8]
$5s7s {}^1\text{S}_0$	23940.054	0.250 [37]
$5s6d {}^3\text{D}_1$	25181.305	0.986 [37]
$5s6d {}^3\text{D}_2$	25186.379	1.708 [37]
$5s8s {}^3\text{S}_1$	26257.057	0.479 [37]
$5s7d {}^3\text{D}_1$	27359.781	0.661 [37]
$5s7d {}^3\text{D}_2$	27365.022	1.145 [37]
$5s9s {}^3\text{S}_1$	27947.012	0.324 [37]
$5s8d {}^3\text{D}_1$	28562.452	0.480 [37]
$5s8d {}^3\text{D}_2$	28565.715	0.831 [37]
$5s10s {}^3\text{S}_1$	28923.469	0.240 [37]
$5s9d {}^3\text{D}_1$	29303.171	0.643 [37]
$5s9d {}^3\text{D}_2$	29303.171	0.371 [37]
$4d^2 {}^3\text{P}_0$	30021.916	1.680 [37]
$4d^2 {}^3\text{P}_1$	30092.384	1.720 [37]
$4d^2 {}^3\text{P}_2$	30226.091	2.210 [37]

Table A.3. Relevant Wavelength and RDMEs for the Excited Manifold for ${}^3\text{P}_2$ of Sr.

State k	ΔE_{ki} (1/cm)	$\langle k D i \rangle$ (a.u.)
$5s4d {}^3\text{D}_1$	3260.000	0.602 [59]
$5s4d {}^3\text{D}_2$	3320.000	2.331 [59]
$5s4d {}^3\text{D}_3$	3421.000	5.530 [59]
$5s4s {}^1\text{D}_2$	5251.000	0.102 [59]
$5s6s {}^3\text{S}_1$	14140.000	4.521 [59]
$5s5d {}^1\text{D}_2$	19829.000	0.365 [59]
$5s5d {}^3\text{D}_1$	20108.000	0.460 [59]
$5s5d {}^3\text{D}_2$	20123.000	1.956 [59]
$5s5d {}^3\text{D}_3$	20146.000	4.994 [59]
$5p^2 {}^3\text{P}_1$	20502.000	2.992 [59]
$5p^2 {}^3\text{P}_2$	20776.000	5.119 [59]
$5p^2 {}^1\text{D}_2$	22062.000	0.682 [59]
$5s7s {}^3\text{S}_1$	22526.000	1.264 [59]

vector light shifts near the focus, introducing an additional dephasing mechanism. We can express this dephasing mechanism via the following Hamiltonian,

Table A.4. Relevant Wavelength and RDMEs for the Excited Manifold in $5s4d\ ^1D_2$.

State k	ΔE_{ki} (1/cm)	$\langle k D i \rangle$ (a.u.)
$5s5p\ ^3P_1$	5645.351	0.186 [83]
$5s5p\ ^3P_2$	5251.141	0.103 [83]
$5s5p\ ^1P_1$	1548.767	1.926 [83]
$4d5p\ ^3F_2$	13117.162	3.010 [83]
$4d5p\ ^3F_3$	13440.029	0.227 [83]
$4d5p\ ^1D_2$	13677.215	6.113 [83]
$5s6p\ ^3P_1$	13718.626	0.671 [83]
$5s6p\ ^3P_2$	13823.381	1.504 [83]
$5s6p\ ^1P_1$	13948.713	2.257 [83]
$4d5p\ ^3D_1$	16114.477	0.062 [83]
$4d5p\ ^3D_2$	16232.053	0.256 [83]
$4d5p\ ^3D_3$	16409.799	0.045 [83]
$4d5p\ ^3P_1$	17153.041	0.060 [83]
$4d5p\ ^3P_2$	17186.915	0.420 [83]
$4d5p\ ^1F_3$	17858.068	0.442 [83]
$5s4f\ ^3F_2$	18600.741	0.073 [83]
$5s4f\ ^3F_3$	18602.713	0.145 [83]
$5s7p\ ^1P_1$	18757.186	1.963 [83]
$5s7f\ ^1F_3$	23513.152	1.431 [85]
$5s9p\ ^1P_1$	23184.739	1.243 [85]
$5s6f\ ^1F_3$	22696.277	1.883 [85]
$5s8p\ ^1P_1$	22318.903	1.591 [85]
$5s5f\ ^1F_3$	21375.167	2.593 [85]
$4d5p\ ^1P_1$	21028.305	1.829 [85]
$5s4f\ ^1F_3$	19394.729	3.576 [85]

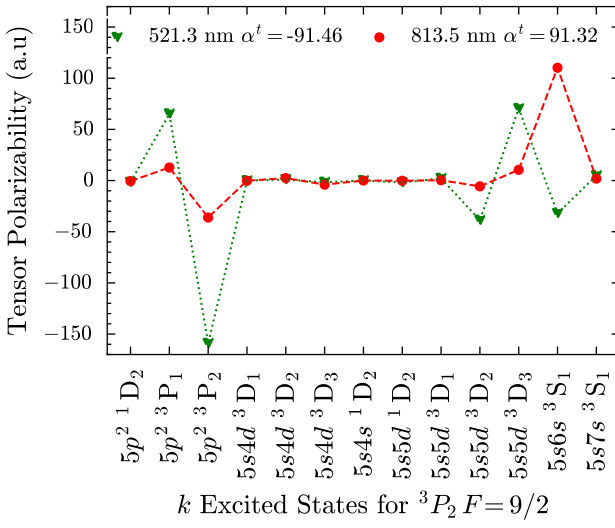


Figure A.1. Contributions of Excited Stats in $5s5p\ ^3P_2$ for Total Tensor Light Shift for 813.5 nm and 521.3 nm. The dashed red line indicates the tensor light shift contributions for 813 nm; each circle represents the total contribution for a given excited state. The dotted green line represents the tensor light shift contributions for 521 nm; each triangle notes the corresponding contributions for each excited states for this wavelength.

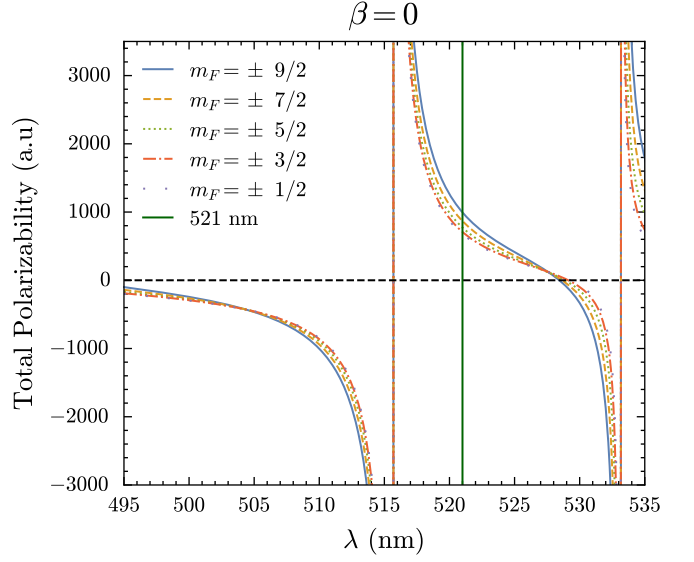


Figure A.2. Contributions of Excited Stats in $5s4d\ ^1D_2$ for Total Light Shift near 521 nm. The solid green indicates 521 nm.

$$H_{\text{VLS}} = \frac{-1}{4} |E_0|^2 i \alpha_e^v(\omega) \frac{\mathbf{C}(r) \cdot \mathbf{F}}{2F} \quad (\text{A6})$$

where $\mathbf{C}(r) = \text{Im}\{\epsilon \times \epsilon^*\}$ corresponds to the circularity of the electric field. Using the vector Debye integrals [90] we compute the corresponding polarization vectors and estimate the scale of the induced light shifts.

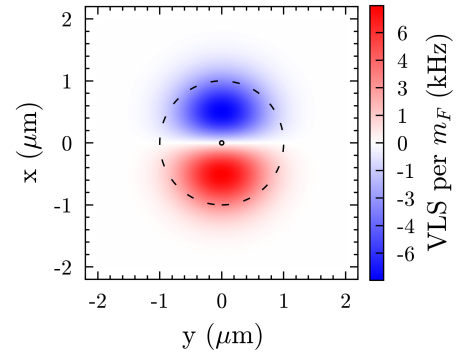


Figure A.3. Polarization Gradient-Induced Vector Light Shifts in Bichromatic Tweezer using 891.5 nm and 518.0 nm for $^{87}\text{Sr}\ ^3P_2$ for $\beta = 0$. We present the vector light shifts per m_F induced by circularity of the electric field near focus. The dashed circle represents the beam waist of 1 micron, while the solid circle represents the position uncertainty, 33 nm, of a qudit in its motional ground state.

In Fig. A.3 we present the total differential vector light shifts per nuclear spin sampled by the atom in its motional ground state at x, y , at $z = 0$. Given the relevant length scale and the symmetry of the vector light shifts, the atom

would sample a light shift maximum of ± 1 kHz per m_F at the edge of this length scale. This effect can be mitigated via dynamical decoupling sequences [7, 91]. Finally, we note that at the center of the tweezer there is effectively no effect due to vector light shifts, ensuring a cancellation of tensor light shifts in 3P_2 .

Appendix B: Tolerances in Bichromatic Tweezers for Yielding State Fidelity of 0.999 in 3P_2 in ${}^{87}\text{Sr}$

In this section we will expand on the framework presented in the paper for estimating tolerances to yield a state fidelity of 0.999.

For large-spin systems such as ${}^{87}\text{Sr}$, and especially for qudit-based applications, it is important to quantify the response of fidelity to power offset and quantization angle by using the Hilbert-Schmidt distance,

$$\mathcal{F} = \frac{1}{d(d+1)} \left(|\text{Tr}\{e^{iH_{\text{Zeeman}}t} e^{-iH_{\text{Realized}}t}\}|^2 + d \right) \quad (\text{B1})$$

Again, we re-introduce the Zeeman Hamiltonian

$$H_{\text{Zeeman}} = g_F \mu_B \vec{B} \cdot \hat{\mathbf{F}} \quad (\text{B2})$$

and the realized Hamiltonian,

$$H_{\text{Realized}} = H_{\text{LS}} + H_{\text{Zeeman}} \quad (\text{B3})$$

In Fig. B.1 we estimate the infidelity of the bichromatic tweezer at x_0 and the corresponding monochromatic tweezers. For monochromatic potentials, the scale of the magnetic field for entering the perturbative regime needed for magic-angle tuning is well within the Paschen-Back regime, in which the $|F, m_F\rangle$ no longer a basis for representing this system. Our fidelity calculations indicate that for high-spin hyperfine manifolds magic-angle tuning is not viable with a monochromatic trapping potential.

Appendix C: Rabi Frequencies in 3P_2

Given the time scale of 1 ms we calculate the scale of the Rabi Frequencies in 3P_2 . We will use the fine structure estimate as a conservative figure of merit for viable coherent excitation rates. In Klüsener et. al. the A coefficient is reported to be 152 μs [7]. To estimate the Rabi frequency they present a relationship between the decay rate A and a reduced matrix element $\langle \gamma_e J_e | H_{\text{ph}}(pL) | \gamma_g J_g \rangle$,

$$A = \frac{16\pi^2 \alpha \nu_0}{2J_e + 1} |\langle \gamma_e J_e | H_{\text{ph}}(pL) | \gamma_g J_g \rangle|^2, \quad (\text{C1})$$

with α the fine structure constant, ν_0 is the frequency of the transition at 671.2 nm (see Fig. 1), $J_e = 2$. Note: this matrix element is *not* to be confused with the absolute value of the M2 $\langle {}^1S_0 | M2 | {}^3P_2 \rangle$, which is $22.6 \mu_B$.

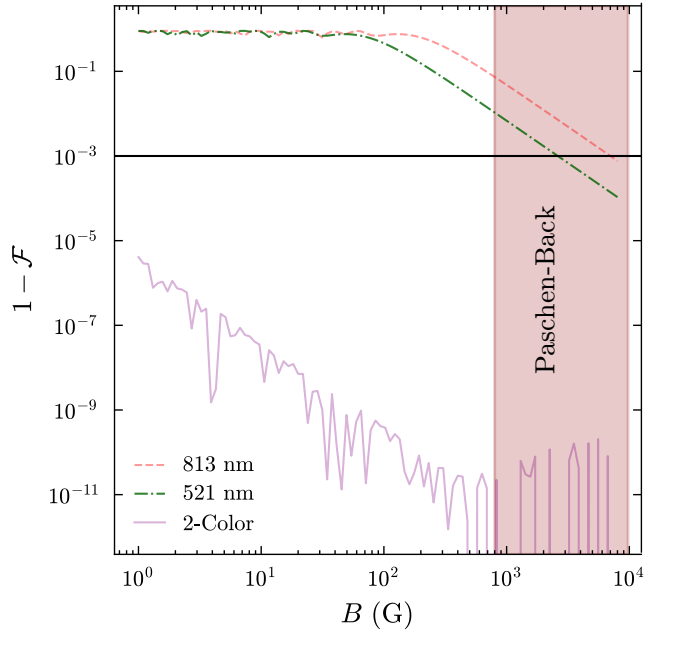


Figure B.1. **State Fidelity as a Function of Magnetic Field Strength for 813.5 nm and 521.3 nm Monochromatic and Bichromatic Tweezer at Tensor Magic Angle.** The solid line represents the state fidelity estimated with the optimal power ratio. The purple line represents the bichromatic tweezer configuration with no power offset (1 mW for each color). The dash-dotted green line represents a trapping potential at 521 nm with equal trap depth to the bichromatic tweezer's. The loosely dashed red a trapping potential at 813 nm with equal trap depth to the bichromatic tweezer's. Finally the blue dashed line represents the target state fidelity of 0.999. The shaded region represents the magnetic fields corresponding to the Paschen-Back regime.

Furthermore, the Rabi frequency is defined as $\Omega = 2\pi E_0 |V_{eg}|/h$, where h is the Planck constant and V_{eg} is,

$$V_{eg} = -\frac{\sqrt{\pi}ec}{2\pi\nu_0} \times \langle \gamma_e J_e | H_{\text{ph}}(0, 2) | \gamma_g J_g \rangle \sum_{\lambda=\pm 1} \lambda d_{0,\lambda}^2(\theta). \quad (\text{C2})$$

where $d_{0,\lambda}^2(\theta)$ is the Wigner d function and the measured value for $\theta = 14^\circ$. Moreover, both Eq. C1 and Eq. C2 and are in SI units.

In Fig. C.1 we present the estimated Rabi frequencies for a beam waist of 10 microns to address each atom in the array. These values indicate the viability of coherent excitation within the 1 ms time scale we used in this paper to yield a state fidelity of 0.999.

Appendix D: Quadratic Zeeman Shift in 5s5p 3P_2

The magnetic sensitivity in 3P_2 introduces a dephasing mechanism via the quadratic Zeeman shift [63]. In this

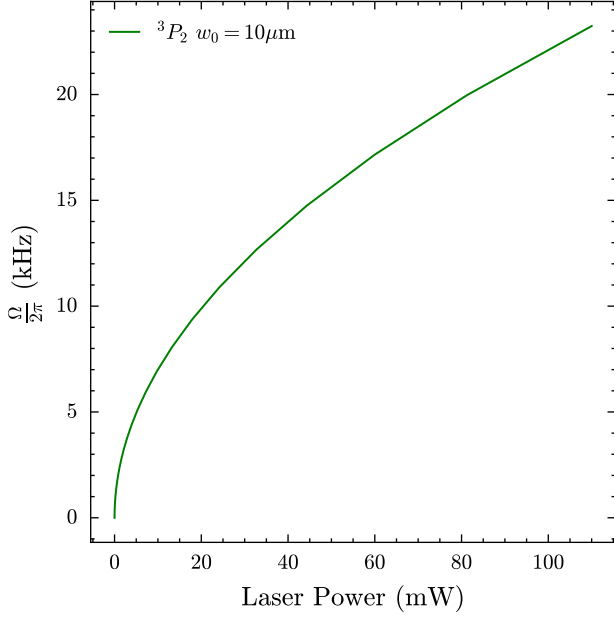


Figure C.1. **Estimated Rabi Rates in ^{87}Sr ${}^3\text{P}_2$ as a Function of Laser Power.** We assume a beam waist of 10 microns.

section we will calculate this effect and its impact on our light shift cancellation scheme. First, let's define the Hamiltonian of interest,

$$H_{\text{total}} = H_Z + A\vec{I} \cdot \vec{J} + Q \frac{\frac{3}{2}\vec{I} \cdot \vec{J}(2\vec{I} \cdot \vec{J} + 1) - IJ(I+1)(J+1)}{2IJ(2I-1)(2J-1)} \quad (\text{D1})$$

where A and Q are the magnetic dipole and quadrupole constants (for $5s5p$ ${}^3\text{P}_2$ $A = -212.765$ MHz and $Q = 67.215$ MHz [92]). Next, we define the Zeeman Hamiltonian H_Z as,

$$H_Z = (g_s S_z + g_l L_z - g_I I_z) \mu_0 B \quad (\text{D2})$$

where the $g_s \approx 2.00232$ and $g_l = 1$ represent the electronic Landé g -factors; $g_I = -131.7712 \times 10^{-6}$ represents measured [93] nuclear Landé g -factor; μ_0 is the Bohr magneton. We note that in this framework we set the magnetic field aligned with the z axis.

Following the formalism presented on Lurio et al. [94] we can write the matrix elements in our chosen basis $|F, m_F\rangle$,

$$\begin{aligned} \langle S' L' J' F' m'_F | H_z | S L J F m_F \rangle = & \delta_{S S'} \delta_{m_F m'_F} (-1)^{F' - m'_F} \begin{pmatrix} F' & 1 & F \\ -m'_F & 0 & m_F \end{pmatrix} \sqrt{(2F'+1)(2F+1)} \\ & \times \left[\delta_{J, J'} (-1)^{I+J+F+1} \begin{Bmatrix} I & F' & J \\ F & I & 1 \end{Bmatrix} \langle I | H_z^n | I \rangle + (-1)^{I+J+F'+1} \begin{Bmatrix} J' & F' & I \\ F & J & 1 \end{Bmatrix} \langle J' | H_z^e | J \rangle \right] \end{aligned} \quad (\text{D3})$$

where the electronic and nuclear reduced elements can be written [95] as,

$$\begin{aligned} \langle J' | H_z^e | J \rangle = & \mu_B B \sqrt{(2J+1)(2J'+1)} \times \left[g_L (-1)^{L+S+J'+1} \begin{Bmatrix} L & J' & S \\ J & L & 1 \end{Bmatrix} \sqrt{L(L+1)(2L+1)} \right. \\ & \left. + g_S (-1)^{L+S+J+1} \begin{Bmatrix} S & J' & L \\ J & S & 1 \end{Bmatrix} \sqrt{S(S+1)(2S+1)} \right] \end{aligned} \quad (\text{D4})$$

$$\langle I | H_z^n | I \rangle = -g_I \sqrt{I(I+1)(2I+1)} \mu_B B \quad (\text{D5})$$

where (\cdot) and $\{\cdot\}$ represent the $3j$ and $6j$ Wigner symbols. Furthermore, in our chosen basis the hyperfine interaction Hamiltonian is diagonal, yielding the following eigenvalues,

$$E_{\text{HFS}}(F) = \frac{A}{2}K + \frac{Q}{4} \frac{\frac{3}{2}K(K+1) - 2I(I+1)J(J+1)}{I(2I-1)J(2J-1)} \quad (\text{D6})$$

$$K = F(F+1) - I(I+1) - J(J+1) \quad (\text{D7})$$

Armed with this framework we pursue the estimation of the quadratic Zeeman shift as follows: we will (1) build

the basis states for the entire manifold (50 in total); (2) iterate through the basis set and apply the rules presented in Eq. (D5) and Eq. (D4) to calculate the Zeeman matrix elements in Eq. (D3); (3) estimate the corresponding hyperfine interaction matrix via Eq. (D7).

In Fig. D.1 we present the Breit-Rabi diagram for $5s5p$ ${}^3\text{P}_2$ manifold in the $|F, m_F\rangle$ basis resulting from the full diagonalization of Eq. (D1). Using the data in the inset of Fig. D.1, we extract a quadratic Zeeman shift of the form:

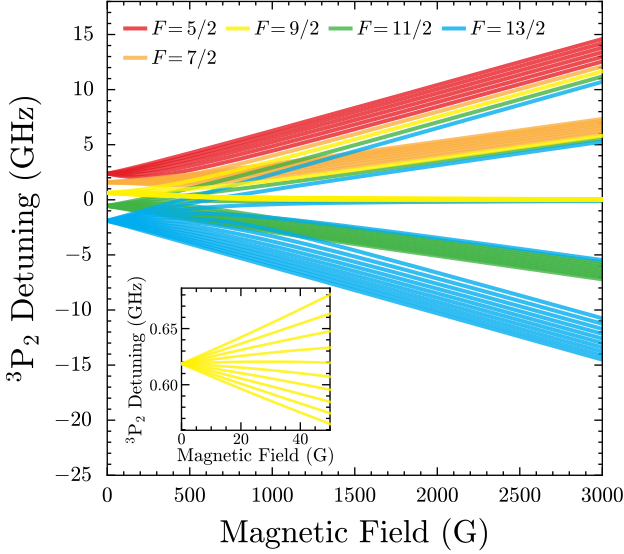


Figure D.1. **Breit-Rabi Diagram for $5s5p\ ^3P_2$ Manifold.** Inset shows the relevant hyperfine manifold of interest, $5s5p\ ^3P_2 F = 9/2$, at the magnetic fields relevant for the calculation of the quadratic Zeeman shift.

$$\Delta_B^2(m_F, B) = (188.7 \text{ Hz}/\text{G}^2) m_F^2 B^2 \quad (\text{D8})$$

Appendix E: Kramers–Heisenberg Formalism

1. Raman Scattering

In this section we present the formalism for calculating Raman and Rayleigh scattering rates. We will follow the formalism laid out in the literature [25, 64]. We will address two types of errors: leakage within the computational manifold and leakages to 3P_0 and 3P_1 .

We start from the Kramers–Heisenberg formula to calculate the scattering rate $\Gamma_{i \rightarrow f}$ of an atom experiencing a transition $i \rightarrow f$: [25, 64]

$$\Gamma_{i \rightarrow f} = \frac{I\omega_{sc}^3}{(4\pi\epsilon_0)^2 c^4 \hbar^3} \frac{8\pi}{3} |\mathbf{D}(\omega)|^2 \quad (\text{E1})$$

where $|\mathbf{D}(\omega)|^2$ is defined as the net induced dipole for the scattered radiation [64]. Induced pumping mechanisms leading to $i \rightarrow j$ correspond to Raman scattering processes, which lead to leakage and depolarization errors in qudits. In contrast, for pumping mechanisms inducing $i \rightarrow i$ events correspond to traditional Rayleigh scattering processes, which lead to dephasing errors.

We can cast the net induced dipole in terms of the polarization degrees of freedom q as,

$$|\mathbf{D}(\omega)|^2 = \sum_{q=-1}^1 |D_q^{(i \rightarrow f)}(\omega)|^2 \quad (\text{E2})$$

Returning to our calculation we will frame Eq. (E1) as,

$$\Gamma_{i \rightarrow f} = \frac{I\omega_{sc}^3}{(4\pi\epsilon_0)^2 c^4 \hbar^3} \frac{8\pi}{3} \sum_{q=-1}^1 |D_q^{(i \rightarrow f)}(\omega)|^2 \quad (\text{E3})$$

The dipole operator for a polarization vector $\hat{\epsilon}$ can be expressed as:

$$d(\epsilon) = \vec{r} \cdot \vec{\epsilon}$$

and for the scattered polarization as

$$d(\epsilon_\lambda) = \vec{r} \cdot \vec{\epsilon}_\lambda$$

where for simplicity we will cast d as the dipole introduced by the incoming radiation and d_λ as the dipole of the scattered photons.

Thus we can write the net dipole as,

$$D_q^{(i \rightarrow f)}(\omega) = \sum_k \left(\frac{\langle f | d_{\lambda,q} | k \rangle \langle k | d_q | i \rangle}{\omega_k - \omega} + \frac{\langle f | d_q | k \rangle \langle k | d_{\lambda,q} | i \rangle}{\omega_k + \omega_{sc}} \right) \quad (\text{E4})$$

where we have casted away the vector nature of the operator encoded in the matrix element. Furthermore we encode the polarization state (in the spherical basis) via q to both incoming and scattered photons [25].

a. π -polarized light

For this calculation we will follow the traditional framework in which we assume the tweezer light to be π polarized (and that is aligned with the quantization axis, $\beta = 0$); thus $d_q \rightarrow d_0$. Moreover, we can express each component of the net induced dipole as a function of the electric dipole d_q driving this process,

$$D_q^{(i \rightarrow f)}(\omega) = \sum_k \left(\langle f | d_{\lambda,q} | k \rangle \frac{\langle k | d_0 | i \rangle}{\omega_{ki} - \omega} + \langle f | d_0 | k \rangle \frac{\langle k | d_{\lambda,q} | i \rangle}{\omega_{ki} + \omega_{sc}} \right) \quad (\text{E5})$$

where we sum over all allowed k excited states. Furthermore, we will define ω_{sc} ,

$$\omega_{sc} = \omega - \omega_{fi} \quad (\text{E6})$$

$$\omega_{fi} = \omega_f - \omega_i \quad (\text{E7})$$

Furthermore, we will cast this formula in terms of scattering amplitudes [26, 27]

$$A_{k,q}^{i \rightarrow j}(\omega) = \left(\langle f | d_{\lambda,q} | k \rangle \frac{\langle k | d_0 | i \rangle}{\omega_{ki} - \omega} + \langle f | d_0 | k \rangle \frac{\langle k | d_{\lambda,q} | i \rangle}{\omega_{ki} + \omega_{sc}} \right) \quad (\text{E8})$$

i represents $|F_1, m_1\rangle$ and f represents $|F_2, m_2\rangle$. For most of our analysis $|F_2, m_2\rangle$ represents states in $5s5p\ ^3P_J$ and $|F_1, m_1\rangle$ represents states in 3P_2 . For the purposes of this calculation $F_1 = ^3P_2$ $F = 9/2$ and F_2 can be presented by either 3P_1 or 3P_0 . Using the Wigner–Eckart theorem,

$$\begin{aligned} \langle F_2, m_2 | d_{\lambda, q} | F', m' \rangle \langle F', m' | d_0 | F_1, m_1 \rangle &= (-1)^{F_2-m_2} \times \\ &\quad \left(\begin{array}{ccc} F_2 & 1 & F' \\ -m_2 & q=0 & m' \end{array} \right) \langle F_2 | d | F' \rangle \times \\ &(-1)^{F'-m'} \times \left(\begin{array}{ccc} F' & 1 & F_1 \\ -m' & q=0 & m_1 \end{array} \right) \langle F' | d | F_1 \rangle \end{aligned} \quad (\text{E9})$$

Using the fact [77, 81, 96],

$$\langle F_2 | d | F' \rangle = (-1)^{F_2-F'} \langle F' | d | F_2 \rangle^* \quad (\text{E10})$$

We note that under that under this framework our RDME is more symmetric under exchange [79],

$$\langle F' | d | F_2 \rangle^* = \langle F' | d | F_2 \rangle \quad (\text{E11})$$

We can decompose the first matrix elements,

$$\begin{aligned} \langle F_2, m_2 | d_{\lambda, q} | F', m' \rangle \langle F', m' | d_0 | F_1, m_1 \rangle &= (-1)^{2F_2-m_2-m'} \\ &\quad \left(\begin{array}{ccc} F_2 & 1 & F' \\ -m_2 & q & m' \end{array} \right) \left(\begin{array}{ccc} F' & 1 & F_1 \\ -m' & q=0 & m_1 \end{array} \right) \langle F' | d | F_2 \rangle \langle F' | d | F_1 \rangle \end{aligned} \quad (\text{E12})$$

where the indexed F_i indicates the appropriate state in which to obtain the reduced dipole matrix elements (RDMEs). Namely, there are two different RDMEs from each manifold considered for a given scattering for the process $F_1 \rightarrow F'$, where F' is a virtual state, with a RDME accounting for that transition, while the secondary process $F' \rightarrow F_2$ to reach the final state requires a different RDME. Similarly, we can compute the second term in the net induced dipole,

$$\begin{aligned} \langle F_2, m_2 | d_0 | F', m' \rangle \langle F', m' | d_{\lambda, q} | F_1, m_1 \rangle &= (-1)^{F_2-m_2} \\ &\quad \left(\begin{array}{ccc} F_2 & 1 & F' \\ -m_2 & q=0 & m' \end{array} \right) \langle F_2 | d | F' \rangle \times \\ &(-1)^{F'-m'} \times \left(\begin{array}{ccc} F' & 1 & F_1 \\ -m' & q & m_1 \end{array} \right) \langle F' | d | F_1 \rangle \end{aligned} \quad (\text{E13})$$

Yielding,

$$\begin{aligned} \langle F_2, m_2 | d_{\lambda, q} | F', m' \rangle \langle F', m' | d_0 | F_1, m_1 \rangle &= (-1)^{2F_2-m_2-m'} \\ &\quad \left(\begin{array}{ccc} F_2 & 1 & F' \\ -m_2 & q=0 & m' \end{array} \right) \left(\begin{array}{ccc} F' & 1 & F_1 \\ -m' & q & m_1 \end{array} \right) \langle F' | d | F_2 \rangle^* \langle F' | d | F_1 \rangle \end{aligned} \quad (\text{E14})$$

Thus we cast the general formula for calculating scattering amplitudes,

$$\begin{aligned} A_{k,q}^{i \rightarrow j}(\omega) &= (-1)^{2F_2-m_2-m'} \langle F' | d | F_2 \rangle \langle F' | d | F_1 \rangle \\ &\quad \left[\frac{1}{\omega_{ki} - \omega} \left(\begin{array}{ccc} F_2 & 1 & F' \\ -m_2 & q & m' \end{array} \right) \left(\begin{array}{ccc} F' & 1 & F_1 \\ -m' & q=0 & m_1 \end{array} \right) \right. \\ &\quad \left. + \frac{1}{\omega_{ki} + \omega_{sc}} \left(\begin{array}{ccc} F_2 & 1 & F' \\ -m_2 & q=0 & m' \end{array} \right) \left(\begin{array}{ccc} F' & 1 & F_1 \\ -m' & q & m_1 \end{array} \right) \right] \end{aligned} \quad (\text{E15})$$

Thus we can write Eq. (E4) in terms of scattering amplitudes,

$$D_q^{(i \rightarrow f)}(\omega) = \sum_k A_{k,q}^{i \rightarrow j}(\omega) \quad (\text{E16})$$

Leading to a compressed Kramers–Heisenberg formula,

$$\Gamma_{i \rightarrow f} = \frac{I \omega_{sc}^3}{(4\pi\epsilon_0)^2 c^4 \hbar^3} \frac{8\pi}{3} \sum_{q=-1}^1 \left| \sum_k A_{k,q}^{i \rightarrow j}(\omega) \right|^2 \quad (\text{E17})$$

b. Arbitrary Linearly Polarized Light

To capture the appropriate scattering rates for our tweezer operating at the magic angle let us cast the polarization vector parametrized by β presented earlier in this paper in the spherical basis as,

$$\boldsymbol{\epsilon}(\beta) = -\frac{\sin \beta}{\sqrt{2}} \hat{\mathbf{e}}_{+1} + \cos \beta \hat{\mathbf{e}}_0 + \frac{\sin \beta}{\sqrt{2}} \hat{\mathbf{e}}_{-1} \quad (\text{E18})$$

Given our choice of arbitrary linear polarization we can write the incoming photon dipole moment as [54],

$$\mathbf{d}_{\lambda, q}(\beta) = -\frac{\sin \beta}{\sqrt{2}} \hat{\mathbf{d}}_{+1} + \cos(\beta) \hat{\mathbf{d}}_0 + \frac{\sin \beta}{\sqrt{2}} \hat{\mathbf{d}}_{-1} \quad (\text{E19})$$

Thus we yield a modified scattering amplitude,

$$\begin{aligned}
A_{k,q}^{i \rightarrow j}(\beta, \omega) = & (-1)^{2F_2 - m_2 - m'} \langle F' \| d \| F_2 \rangle \langle F' \| d \| F_1 \rangle \\
& \times \left\{ \frac{1}{\omega_{ki} - \omega} \left[\left(\begin{array}{ccc} F_2 & 1 & F' \\ -m_2 & q & m' \end{array} \right) \left(\begin{array}{ccc} F' & 1 & F_1 \\ -m' & q=0 & m_1 \end{array} \right) \cos \beta + \left(\begin{array}{ccc} F_2 & 1 & F' \\ -m_2 & q & m' \end{array} \right) \left(\begin{array}{ccc} F' & 1 & F_1 \\ -m' & q=-1 & m_1 \end{array} \right) \frac{\sin \beta}{\sqrt{2}} \right. \right. \\
& \quad \left. \left. - \left(\begin{array}{ccc} F_2 & 1 & F' \\ -m_2 & q & m' \end{array} \right) \left(\begin{array}{ccc} F' & 1 & F_1 \\ -m' & q=1 & m_1 \end{array} \right) \frac{\sin \beta}{\sqrt{2}} \right] \right. \\
& \quad \left. + \frac{1}{\omega_{ki} + \omega_{sc}} \left[\left(\begin{array}{ccc} F_2 & 1 & F' \\ -m_2 & q=0 & m' \end{array} \right) \left(\begin{array}{ccc} F' & 1 & F_1 \\ -m' & q & m_1 \end{array} \right) \cos \beta + \left(\begin{array}{ccc} F_2 & 1 & F' \\ -m_2 & q=-1 & m' \end{array} \right) \left(\begin{array}{ccc} F' & 1 & F_1 \\ -m' & q & m_1 \end{array} \right) \frac{\sin \beta}{\sqrt{2}} \right. \right. \\
& \quad \left. \left. - \left(\begin{array}{ccc} F_2 & 1 & F' \\ -m_2 & q=1 & m' \end{array} \right) \left(\begin{array}{ccc} F' & 1 & F_1 \\ -m' & q & m_1 \end{array} \right) \frac{\sin \beta}{\sqrt{2}} \right] \right\} \quad (E20)
\end{aligned}$$

We are interested in yielding a general framework in which to calculate Raman scattering errors of the form $|^3P_2, F, m_F \rangle \rightarrow |^3P_J, F', m_{F'} \rangle$ where $5s5p$ 3P_J corresponds to 3P_1 , 3P_0 and 3P_2 . This framework will allow us to estimate scattering rates for leakages into other metastable states as well within 3P_2 .

2. Rayleigh Decoherence via Differential Scattering Amplitudes between m_F

In addition to Raman scattering, far-detuned light fields can induce Rayleigh scattering. The literature defines elastic Rayleigh scattering as [26],

$$\Gamma_{el}^{i,j}(\omega) = \frac{I\omega^3}{(4\pi\epsilon_0)^2 c^4 \hbar^3} \frac{8\pi}{3} \sum_q \left(\sum_k A_{k,q}^{i \rightarrow i}(\omega) - A_{k,q}^{j \rightarrow j}(\omega) \right)^2 \quad (E21)$$

Furthermore, let's define effective differential scattering amplitude between nuclear spins,

$$\epsilon(\omega) = \sum_q \left(\sum_k A_{k,q}^{i,i}(\omega) - \sum_k A_{k,q}^{j,j}(\omega) \right) \quad (E22)$$

Thus we can see that dephasing errors scale quadratically [26],

$$\Gamma_{el}^{i,j}(\omega) = \frac{I\omega^3}{(4\pi\epsilon_0)^2 c^4 \hbar^3} \frac{8\pi}{3} \left[\epsilon(\omega) \right]^2 \quad (E23)$$

For this form of error the difference in phase between the scattering amplitudes of i, j nuclear spins lead to constructive interference driving dephasing. For clarity, we will expand this expression (and adding β as a parameter) to,

$$\Gamma_{el}^{i,j}(\beta, \omega) = \frac{I\omega^3}{(4\pi\epsilon_0)^2 c^4 \hbar^3} \frac{8\pi}{3} \sum_q \left[\left(\sum_k A_{k,q}^{i \rightarrow i}(\beta, \omega) \right)^2 + \left(\sum_k A_{k,q}^{j \rightarrow j}(\beta, \omega) \right)^2 - 2 \sum_k A_{k,q}^{i \rightarrow i}(\beta, \omega) A_{k,q}^{j \rightarrow j}(\beta, \omega) \right] \quad (E24)$$

The first two terms represent standard Rayleigh scattering for i, j nuclear spins in the qudit. However, the last term represents the overlap between the scattering amplitudes of the different nuclear spins, introducing a decoherence mechanism driving depolarization errors.

For qubit-systems, characterizing dephasing via this formalism is straight-forward. For qudits we need to expand this formalism by introducing \mathcal{E} , a matrix representing the elastic Rayleigh scattering in the $SU(10)$ manifold.

$$\mathcal{E} = \begin{pmatrix} 0 & \Gamma_{el}^{-9/2, -7/2} & \Gamma_{el}^{-9/2, -5/2} & \Gamma_{el}^{-9/2, -3/2} & \dots & \Gamma_{el}^{-9/2, 7/2} & \Gamma_{el}^{-9/2, 9/2} \\ \Gamma_{el}^{-7/2, -9/2} & 0 & \Gamma_{el}^{-7/2, -5/2} & \Gamma_{el}^{-7/2, -3/2} & \dots & \vdots & \vdots \\ \Gamma_{el}^{-5/2, -9/2} & \Gamma_{el}^{-5/2, -7/2} & 0 & \ddots & \dots & \vdots & \vdots \\ \Gamma_{el}^{-3/2, -9/2} & \Gamma_{el}^{-3/2, -7/2} & \ddots & \ddots & \ddots & \vdots & \vdots \\ \vdots & \vdots & \Gamma_{el}^{i,j} & \ddots & 0 & \vdots & \vdots \\ \Gamma_{el}^{7/2, -9/2} & \Gamma_{el}^{7/2, -7/2} & \vdots & \dots & \dots & 0 & \Gamma_{el}^{7/2, 9/2} \\ \Gamma_{el}^{9/2, -9/2} & \Gamma_{el}^{9/2, -7/2} & \Gamma_{el}^{9/2, -5/2} & \dots & \Gamma_{el}^{9/2, 5/2} & \Gamma_{el}^{9/2, 7/2} & 0 \end{pmatrix} \quad (E25)$$

From \mathcal{E} we define the effective Rayleigh scattering rate for a nuclear spin as,

$$\Gamma_{\text{eff}}(j) = \frac{1}{n} \sum_{i=1}^n \mathcal{E}_{ij} \quad (E26)$$

In Eq. (E26) j is the column index representing nuclear spin.